Mineralogy and Petrology (2021) 115:687–708
https://doi.org/10.1007/s00710-021-00762-y

ORIGINAL PAPER

Petrogenesis of Early Paleozoic adakitic granitoids in the eastern Qilian Block, northwest China: implications for the South Qilian Ocean subduction

Jiao-Long Zhao[1] · Bin Wu[2] · Xin Zhang[3] · Wan-Feng Chen[1] · Xiao-Xiao Ma[1]

Received: 23 March 2021 / Accepted: 30 July 2021 / Published online: 27 August 2021

Abstract

The geodynamic mechanism responsible for the generation of Early Paleozoic magmatism within the Qilian Block, northwest China, remains controversial. In this paper, we present new geochronological, mineralogical, and geochemical data for the Hejiashan (HJS) granite and Lajishan (LJS) quartz diorite from the eastern Qilian Block, to constrain their origin and the regional evolutionary history. Laser abalation–inductively coupled plasma–mass spectrometry (LA–ICP–MS) zircon U–Pb dating results show that the HJS granites and LJS quartz diorites were emplaced between 445 and 438 Myr ago. The HJS granites are high-K calc-alkaline, metaluminous to weakly peraluminous, with K_2O/Na_2O weight ratios of 0.84–1.12. The LJS quartz diorites are calc-alkaline and metaluminous with K_2O/Na_2O weight ratios of 0.34–0.46. Both have similar whole-rock Sr–Nd isotopic compositions. They are characterized by low heavy rare earth elements (HREEs) and Y concentrations, and high Sr/Y and La/Yb ratios, similar to adakitic rocks. Notably, the LJS quartz diorites are more depleted in HREEs and Y, and have much higher Mg# [$=100\times Mg/(Mg+Fe)$], La/Yb, Sr/Y, and zircon $\varepsilon_{Hf}(t)$ values, and MgO, Cr, Co and Ni concentrations than those of the HJS granites. The HJS granites were most likely derived from partial melting of a thickened juvenile lower crust with amphibole and minor plagioclase as residual phases in the magma source. Conversely, the LJS quartz diorites were produced by partial melting of the subducted oceanic slab and minor sedimentary materials in the garnet and rutile stability field. Combined data from this and previous studies suggest that the Early Paleozoic magmatism within the Qilian Block mainly occurred ca. 464–402 Myr ago as a response to post-collisional extension. Break-off of the northward subducted South Qilian oceanic slab after continental collision between the Qaidam and Qilian Blocks was the primary dynamic mechanism responsible for the Early Paleozoic extensive crust-mantle interaction and magmatism within the Qilian Block.

Keywords Early Paleozoic · Petrogenesis · Post-collisional extension · Slab break-off · Qilian Block

Introduction

Adakites are a special type of igneous rocks and were originally defined as a group of intermediate–felsic igneous rocks derived from partial melting of a young and hot basaltic slab in modern subduction zones (Defant and Drummond 1990). Geochemically, adakite is characterized by depletions in Y and heavy rare earth elements (HREEs), high Sr/Y and La/Yb ratios, and a lack of significant negative Eu anomaly (Castillo 2012; Chung et al. 2003). Currently, the term "adakite" is used for a much wider range of magmatic rocks than originally defined (Ma et al. 2016). Some rocks with adakitic affinity are considered to be apparently derived from continental crust and usually called "adakitic" or "C-type (continental)" rocks (Ma et al. 2015b; Xu et al. 2002; Zhang et al.

Editorial handling: X. Xu.

✉ Jiao-Long Zhao
jlz@lzu.edu.cn

[1] School of Earth Sciences, Key Laboratory of Mineral Resources in Western China (Gansu Province), Lanzhou University, Chengguan District, No.222 South Tianshui Road, Lanzhou 730000, China

[2] State Key Laboratory of Nuclear Resources and Environment, East China University of Technology, No.418 Guanglan Road, Qingshanhu District, Nanchang 330013, China

[3] College of Resources and Environmental Science, Ningxia University, Xixia District, No.539 Helanshan Road, Yinchuan 750021, China

2001); all of these terms are simplistically referred to as "adakitic rocks" in this manuscript. Alternative geodynamic models have also been suggested to explain the origins of adakitic rocks, including (1) melting of a thickened lower crust (Atherton and Petford 1993; Chung et al. 2003), (2) partial melting of a delaminated lower crust (Gao et al. 2004; Xu et al. 2002), (3) fractional crystallization of water-rich arc basaltic magmas (Castillo et al. 1999; Dai et al. 2017; Macpherson et al. 2006), and (4) magma mixing between basaltic and felsic magmas (Chen et al. 2013; Streck et al. 2007). The origin of adakite magmatism is thought to be of particular importance for understanding the Archean crustal evolution because of their compositional similarity to Archean TTGs (Tonalite–Trondhjemite–Granodiorite) (Martin et al. 2005). In particular, melts derived from an oceanic crustal source may be important in contributing to crustal growth (Eyuboglu et al. 2011; Huang et al. 2015; Song et al. 2014a, b). On the other hand, their distinctive geochemical signatures suggest that their generation likely occurred within the garnet and/or amphibole stability fields, reflecting high-pressure processes. Consequently, adakitic rocks could provide significant information on crustal evolution and the evolutionary histories of orogenic belts.

The Qilian orogenic belt located on the northern margin of the Qinghai-Tibet Plateau in western China has recorded a complex history of typical collisional orogenies (Fig. 1a). This belt is composed of the North Qilian Orogenic Belt, the Qilian Block, and the North Qaidam ultrahigh-pressure metamorphic (NQ-UHPM) belt (Fig. 1a). The intense and widespread early Paleozoic magmatic rocks in the Qilian orogeny have been suggested to be products of the subduction of oceanic crust and the subsequent continental collision (Li et al. 2017; Song et al. 2013, 2014a, b; Wang et al. 2018). It is generally accepted that the northward subduction of the North Qilian oceanic lithosphere resulted in the development of a Western Pacific-type trench–arc–back-arc-basin system of the North Qilian Orogenic Belt (Li et al. 2017; Song et al. 2013; Wang et al. 2018, 2019). Numerous studies also suggest that the North Qilian oceanic lithosphere simultaneously subducted southwards beneath the Qilian Block, and induced the intensely granitoidic magmatism within the Qilian Block (Chen et al. 2008; Li et al. 2017; Tung et al. 2016). However, the eclogites of the mid-ocean ridge basalt (MORB) protolith in the NQ-UHPM belt indicate the presence of another ocean basin located between the Qilian and the Qaidam Blocks. Therefore, some authors have recently suggested that Early Paleozoic magmatism within the Qilian Block may have been induced by the northward subduction of this oceanic slab beneath the Qilian Block and the subsequent continental collision between the Qilian and the Qaidam Blocks (Gao et al. 2018; Huang et al. 2015; Yang et al. 2015, 2016, 2018). As such, the tectonic evolution and the geodynamic mechanism responsible for the generation of the Qilian orogeny remains controversial. As the critical junction of the North Qilian Orogenic Belt and the NQ-UHPM belt, the Qilian Block occupies a crucial place for understanding the tectonic evolution of the Qilian orogenic belt. The Early Paleozoic granitoids in the Qilian Block are composed of voluminous I- and S-type granitoids and adakitic rocks (Huang et al. 2015; Song et al. 2014a, b; Tung et al. 2016; Yang et al. 2015, 2016; Yong et al. 2008). Previous studies have suggested that the Early Paleozoic adakitic rocks in Qilian Block are widely distributed and mainly derived from partial melting of a thickened lower crust (Huang et al. 2015; Tung et al. 2016). However, these slab-derived adakites are sparse, and few studies have been conducted on the petrogenesis and tectonic significance of these plutonic rocks. In this study, we provide a combined mineralogical, geochronological, and geochemical data for the newly identified Lajishan (LJS) and Hejiashan (HJS) adakitic plutons from the eastern Qilian Block (Fig. 1a). By integrating the new results and previous data, we aim to provide close constraints on the magma source and petrogenesis of these granitoids and to shed new light on the tectonic evolution of the Qilian orogeny during the Early Paleozoic.

Geological setting

The Qilian orogenic belt is a composite orogenic belt (Fig. 1a; Song et al. 2013; Xia et al. 2016). The northern North Qilian Orogenic Belt is a typical western Pacific-type trench–arc–back-arc system and characterized by the occurrence of low-T/HP blueschist and eclogite-facies rocks (Song et al. 2009). From north to south, it can be divided into the northern back-arc ophiolite belt, the middle arc magmatic belt, and the southern ophiolite belt (Fig. 1a).

The Qilian Block, bounded by the NQ-UHPM belt and West Qinling Orogenic belt to the south and the North Qilian Orogenic Belt to the north, consists predominantly of Precambrian metamorphic basement overlain unconformably by supracrustal Phanerozoic strata (Li et al. 2018; Wan et al. 2003; Wang et al. 2016). Abundant Early Paleozoic granitoids are exposed in the eastern section of the Qilian Block, with crystallization ages in the range 517–402 Ma. They are composed of adakitic granitoids, I- and S-type granitoids, and minor plagiogranites, and are considered to be the result of oceanic subduction and subsequent continental collision (Huang et al. 2015; Peng et al. 2017; Qin et al. 2014; Wu et al. 2010; Tung et al. 2016; Yang et al. 2015). Mesozoic magmatism is rare and only exposed in the southeastern-most part of the Qilian Block (Li et al. 2017). The NQ-UHPM belt is dominated by paragneisses and orthogneisses intercalated with blocks of eclogite, granulite, and peridotites (Song et al. 2014a, b; Yang et al. 1998). Granitoids in this belt are generally coeval with those exposed in the Qilian Block, with ages in the range from 493 to 370 Ma (Huang et al. 2015).

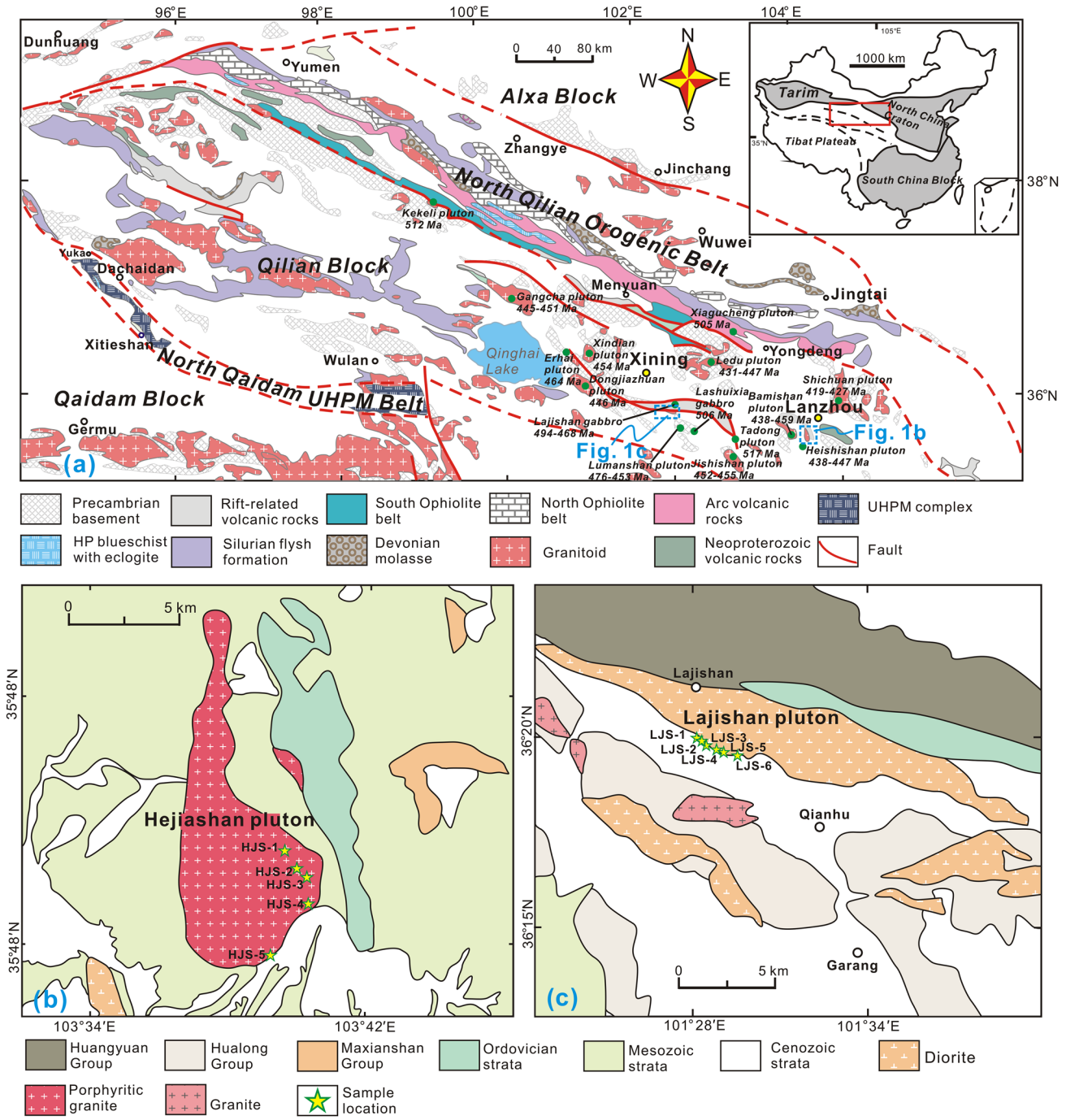

Fig. 1 (**a**) Geological sketch map of the Qilian orogenic belt with the localities of major granitoids and their ages (modified from Xia et al. 2016), data are from the references quoted in Table S1. (**b**) Geological map of the Hejiashan (HJS) granitic pluton (modified after Yang et al. 2015). (**c**) Geological map of the Lajishan (LJS) pluton (modified after Fu et al. 2014)

Both the HJS and LJS plutons are located along the southern margin of the Qilian Block. The HJS pluton crops out in northeast Lintao Country, Gansu Province (Fig. 1b). It intrudes into the Ordovician volcanic-sedimentary strata and is overlain by the Mesozoic Hekou Group. The pluton is mainly composed of coarse-grained granites and subordinate medium-grained granodiorites (Fig. 2a). The coarse-grained granites are light pink and have equigranular–porphyritic textures with 10–15 vol% phenocrysts of alkali feldspar (3–12 mm) and minor plagioclase and quartz (Fig. 2c and d). The groundmass is fine-grained, and consists mainly of alkali feldspar, quartz, plagioclase, biotite and amphibole

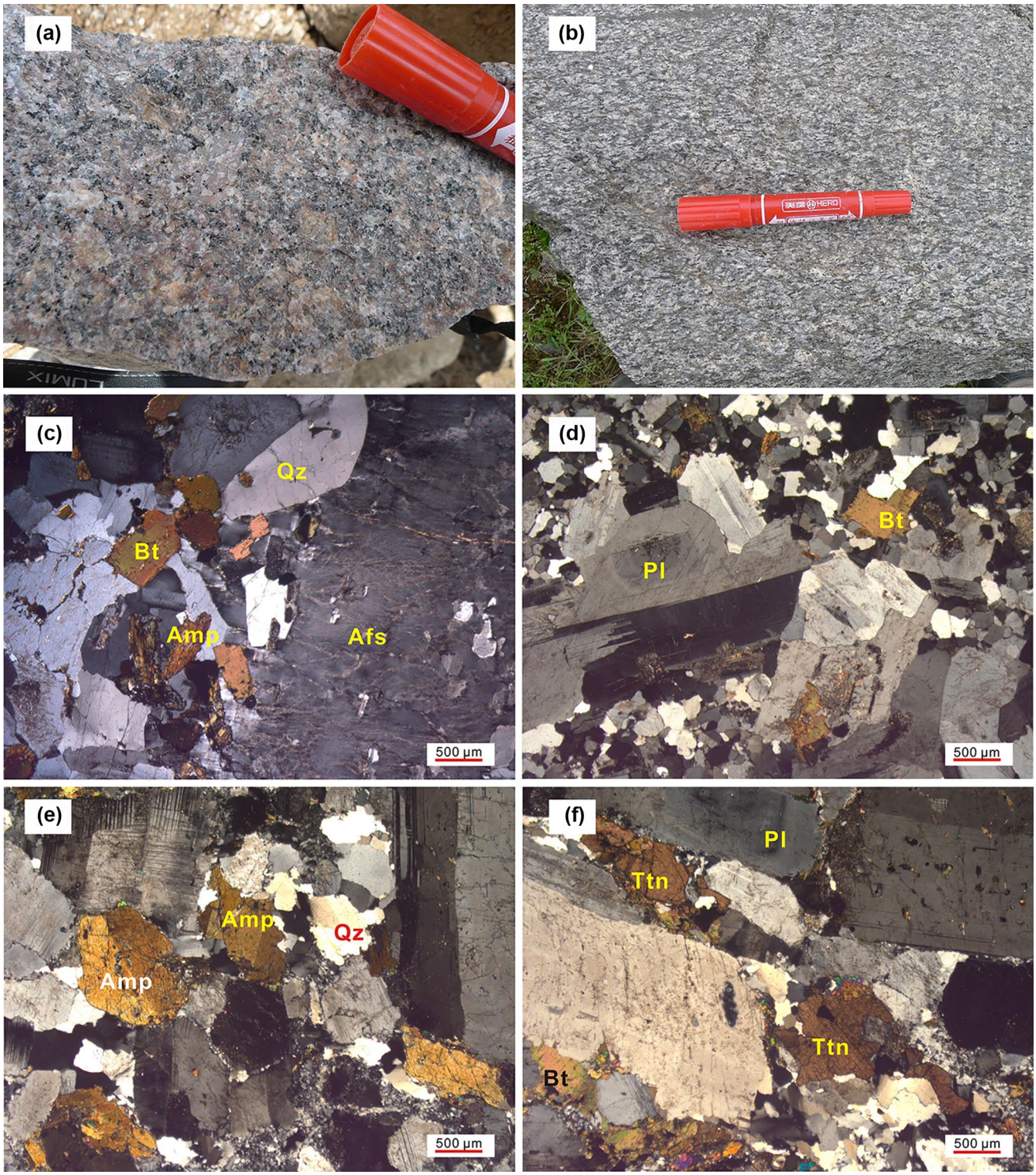

Fig. 2 Images of HJS and LJS adakitic granitoids. (**a**) Field photograph of HJS granitoid specimen. (**b**) Field photograph of LJS granitoid specimen. (**c, d**) Cross-polarised, transmitted-light images of granites from the HJS pluton. (**e, f**) Cross-polarised, transmitted-light images of granitoids from the LJS pluton. Abbreviations of mineral names accroding to Whitney and Evans (2010): Qz – quartz; Afs – alkali feldspar; Pl – plagioclase; Bt – biotite; Amp – amphibole; Ttn – titanite

with minor zircon, and titanite. Alkali feldspar phenocrysts are euhedral to subhedral crystals, frequently enclosing plagioclase and euhedral amphibole crystals. Plagioclases are euhedral to subhedral with lamellar twinning, which occasionally show concentric zoning (Fig. 2d). Biotite occurs as anhedral–subhedral blades. Amphiboles are relatively unaltered and are subhedral to euhedral (Fig. 2c).

The LJS pluton, located in the central region of the Qi(lian)-Qin(ling) Accretionary belt, is ~ 25 km long and ~ 1–5 km wide along the Lajishan rift-related volcanic rock belt (Fig. 1c). This pluton intruded into the Precambrian Huangyuan group and the Ordovician volcanic-sedimentary strata. It consists predominantly of quartz diorites that are fine- to medium-grained (Fig. 2b) and consists of plagioclase (40–45 vol%), alkali feldspar (5–10 vol%), quartz (10–15 vol%), amphibole (15–20 vol%), and biotite (5–10 vol%). Minor accessory minerals include zircon, titanite, epidote, and Ti–Fe oxides. Plagioclase usually occurs as subhedral–euhedral laths with well-developed twinning and/or concentric zoning. Amphibole is euhedral to subhedral and displays characteristic yellowish to green pleochroism (Fig. 2e), indicative of primary magmatic origin. Biotite varies in form from anhedral grains to subhedral blade-shaped crystals. Titanite within the intrusion typically occurs as interstitial to quartz and plagioclase (Fig. 2f), suggesting late crystallization.

Sample materials and analytical methods

Sampling and specimen preparation

Samples weighing ~ 5 kg each were collected during fieldwork in 2017, and detailed sampling locations are presented in (Fig. 1b and c). Selected fresh whole-rock samples were crushed and powdered to 200 mesh in an agate ring mill for whole-rock geochemical analyses. Three samples in this study, HJS-2 (35°50′13"N, 103°40′32"E) for the HJS pluton and LJS-1 (36°19′59"N, 101°28′07"E) and LJS-3 (36°19′55"N, 101°28′21"E) for the LJS pluton, were selected for zircon U–Pb dating. Zircon grains were separated by standard density and magnetic techniques, and then selected by hand under a binocular microscope. Representative zircon grains were mounted in epoxy resin, and ground and polished to expose grain interiors. For electron probe micro-analyser (EPMA) measurements, polished mounts were coated with carbon for conductivity.

Zircon U–Pb dating and Hf isotopes

Cathodoluminescence (CL) images of zircons found within the samples were obtained using a a JSM-6510 scanning electron microscope equipped with Gatan Mini CL. Zircon U–Pb isotopic analyses were carried out using an Agilent ICP–MS system coupled to a New Wave Research 213 nm laser ablation system. Analyses were carried out using a beam diameter of 32 μm, a repetition rate of 5 Hz, and an energy of 23.74–26.68 J/cm^2. A homogeneous reference zircon (GEMOC GJ-1, Jackson et al. 2004) was used to correct the mass discrimination of the mass spectrometer and residual elemental fractionation. A well-characterized reference zircon Mud Tank (Black and Gulson 1978) was used as an independent control on reproducibility and instrument stability. In this study, measurements of the reference zircon GJ-1 (^{206}Pb/^{238}U age of 599.8 ± 4.5 Ma; Jackson et al. 2004) and Mud Tank (^{206}Pb/^{238}U age of 732 ± 5 Ma; Black and Gulson 1978) gave ^{206}Pb/^{238}U ages of 600 ± 3 Ma (n = 15) and 728 ± 4 Ma (n = 5), respectively, all of which are consistent with the recommended values. The raw ICP–MS U–Pb isotopic data were acquired using GLITTER 4.4 (Griffin et al. 2008), using the method for common Pb described by Andersen (2002). Mean age calculations were performed, and Wetherill Concordia plots were drawn, using Isoplot 3.00 (Ludwig 2003).

In-situ zircon Hf isotope analyses were conducted on the same spots as the U–Pb age determinations. Hf isotopic compositions were determined with a Neptune Plus multi-collector (MC) ICP–MS system coupled to a Geolas HD excimer ArF laser ablation system. Zircon grains were ablated with a beam diameter of 44 μm. Detailed operating conditions for the laser ablation system and the MC–ICP–MS instrument and analytical method are the same as description by Hu et al. (2012). Off-line selection and integration of analyte signals, and mass bias calibrations were performed using ICPMSDataCal 11.8 (Liu et al. 2010a). The reference zircon 91,500 was used for time-drift correction and external calibration. In this study, measurements of the reference zircon 91,500 gave ^{176}Hf/^{177}Hf ratios of 0.282304 ± 0.000008 (n = 20), consistent with recommended values within 2σ errors (0.282307 ± 31, Wu et al. 2006).

Mineral major-element analyses

Mineral major-element compositions were determined with a JEOL JXA-8100 EPMA system operated at 15 kV and 20 nA, with a beam diameter of 1 μm. Peaks counting times were 10 s for Si, Al, Mg, Ca, Mn, Fe, Na, and F, and 20 s for Ti; backgrounds were measured for half of the respective peak counting time. For all elements the Kα lines were analyzed. The following reference materials were used: rutile (Ti), pyrophanite (Mn), jadeite (Na, Si), topaz (Al, F), magnetite (Fe), plagioclase (Ca), olivine (Mg), and sanidine (K). A ZAF correction was applied to the data. The analytical uncertainties were < 1% for major elements and < 10% for trace elements.

Whole-rock major and trace element, and Sr–Nd isotope analyses

For major-element analyses, mixtures of whole-rock powders (0.5 g) and $Li_2B_4O_7 + LiBO_2 + LiBr$ (11 g) were made into glass discs and then analyzed using a Thermo Scientific ARL 9900 X-ray fluorescence (XRF) spectrometer. The analytical precision was estimated to be less than 10% for all major elements, and less than 1% for the majority of elements. Trace element concentrations were determined using a Finnigan Element II ICP–MS system. Detailed analytical procedures followed Gao et al. (2003). The analytical precision was better than 10% for all trace elements, with the majority being better than 5%.

Geological rock powder was decomposed by high-pressure polytetrafluoroethylene (PTFE) bombs. Sr and Nd were both purified from the same digestion solution by two steps column chemistry. The first exchange column combined with BioRad AG50W × 8 and Sr Spec resin was used to separate Sr and REE from the sample matrix. Nd was separated from the other REE on the second column with an Ln Spec-coated Teflon powder. The Sr- and Nd-bearing solution was then dried and re-dissolved in 1.0 ml 2 wt% HNO_3. Small aliquots of each re-dissolved sample were analyzed using a Agilent Technologies 7700 × quadrupole ICP–MS system to determine the exact contents of Sr and Nd elements. Diluted solutions (50 ppb Sr and 50 ppb Nd) were introduced into a Nu Instruments Nu Plasma II MC–ICP–MS device by Teledyne Cetac Technologies Aridus II desolvating nebulizer system.

The isotopic ratio raw data were corrected for mass fractionation by normalizing to $^{86}Sr/^{88}Sr = 0.1194$ for Sr and $^{146}Nd/^{144}Nd = 0.7219$ for Nd. Isotopic standards (NIST SRM 987 for Sr and JNdi-1 for Nd) were periodically analyzed to correct instrumental drift. Geochemical reference materials of USGS AVG-2 and STM-2 (Table S7) were treated as quality control.

Results

Zircon U–Pb ages

Zircons from the granitic plutons in this study are transparent, colorless to pale yellow, euhedral, and prismatic with well-developed oscillatory zoning in the CL images (Fig. 3). They range from 50 to 100 μm in length, with length/width ratios of 1:1–2:1. The zircon grains used for LA–ICP–MS analysis contain similar Th and U concentrations (generally 234–603 ppm and 271–913 ppm, respectively) and have relatively high Th/U ratios (0.48–1.40), indicating magmatic origin (Corfu et al. 2003; Wu and Zheng 2004). The results of the LA–ICP–MS U–Pb isotopic analyses are listed in Table S2 and shown in Fig. 3.

Fifteen U–Pb zircon analyses from the sample HJS-2 provided concordant $^{206}Pb/^{238}U$ ages that range from 450 ± 6 to 435 ± 5 Ma with a weighted mean age of 444.6 ± 2.6 Ma [mean square weighted deviation (MSWD) = 0.88, Fig. 3a]. This age represents the crystallization age of the HJS granite.

Two samples, LJS-1 and LJS-3, from the LJS pluton were analyzed during this study. Fourteen analyses of zircons from sample LJS-1 are all concordant or near-concordant, and yield a weighted mean $^{206}Pb/^{238}U$ age of 438.0 ± 2.7 Ma (MSWD = 1.1, Fig. 3b). Eighteen analyses from sample LJS-3 form a concordant group, with a weighted mean $^{206}Pb/^{238}U$ age of 443.0 ± 3.1 Ma (MSWD = 1.3, Fig. 3c). These two ages are within error, indicating a crystallization age of 440 Ma for the LJS quartz diorite.

Chemical composition of minerals

Results of representative EPMA chemical analyses of plagioclase, biotite, amphibole, and Fe-Ti oxide within the granitoids in this study are listed in Table S3–S5 and shown in Fig. 4. Plagioclase crystals in both the HJS granite and LJS quartz diorite have similar compositions, with high contents of Ab (68–80), minor amounts of An (18–29), and Or (0.3–3), and are classified as oligoclase (Fig. 4a).

Biotite grains in the HJS granite have relatively high FeO^T (total Fe expressed as Fe^{2+} oxide; 18.86–19.04 wt%) and K_2O (8.21–8.51 wt%), and low MgO (10.71–11.02 wt%) contents, with high $FeO^T/(FeO^T + MgO)$ ratios of 0.63–0.64. Biotite grains in the LJS quartz diorite have high MgO (14.67–15.29 wt%) and low FeO^T (15.94–16.24 wt%), and TiO_2 (1.53–1.61 wt%) contents with relatively low $FeO^T/(FeO^T + MgO)$ ratios (0.52). In the Mg–($Al^{VI} + Fe^{3+} + Ti$)–($Fe^{2+} + Mn$) diagram, all biotite specimens from the HJS and LJS plutons are classified as magnesiobiotite (Fig. 4b).

All amphibole crystals in the HJS and LJS plutons are compositionally uniform without zoning. Amphiboles in the HJS granite have relatively high FeO^T (16.03–16.76 wt%) and low MgO (11.53–12.69 wt%), whereas the amphiboles in the LJS quartz diorite show slightly lower FeO^T (13.4–14.63 wt%) and higher MgO (12.86–14.17 wt%), Al_2O_3 (7.08–8.49 wt%) and TiO_2 (0.98–1.42 wt%). Both have high but restricted CaO (9.97–11.24 wt%) contents with Ca_B values of > 1.5 and $(Na + K)_A < 0.50$, and thus are calcic amphiboles. They also exhibit intermediate SiO_2 contents and high $Mg/(Mg + Fe^{2+})$ values, and could therefore be further classified as magnesiohornblende using the classification of Leake et al. (1997) (Fig. 4c). Furthermore, the amphiboles in both plutons have low $Fe/(Fe + Mg)$ and high $Fe^{3+}/(Fe^{2+} + Fe^{3+})$ ratios, indicating crystallization under relatively high oxygen fugacity.

The Fe-Ti oxides are abundant in the LJS quartz diorite and generally have intergrowth relationships with the amphibole grains. They are uniform in composition and predominantly consist of FeO^T (94.35–95.23 wt%) with minor TiO_2 (0.04–0.06 wt%) and MnO (0.15–0.94 wt%), typical of magnetite.

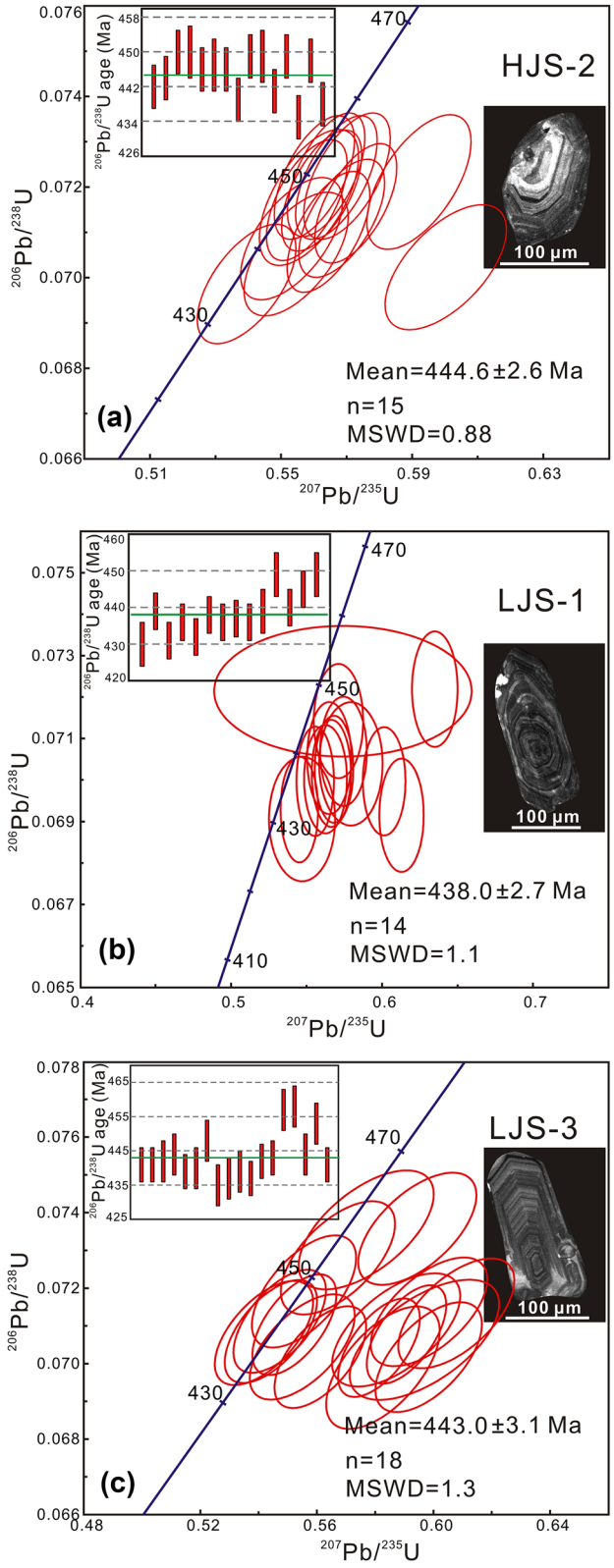

Fig. 3 CL images of representative zircon grains, Wetherill Concordia plots and weighted mean $^{206}Pb/^{238}U$ ages for granitoidic rocks of the HJS pluton (**a**) and LJS pluton (**b**–**c**)

Whole-rock major and trace element geochemistry

The major and trace element compositions of representative samples from the HJS and LJS plutons are given in Table 1. All samples from the HJS pluton show limited chemical variation, and have an acidic signature and relatively high alkali contents, which fall in the granite field and subalkaline series on a total alkali versus silica plot (Fig. 5a). They are enriched in K_2O with K_2O/Na_2O weight ratios of 0.84–1.12 and can be classified as high-K calc-alkaline rocks (Fig. 5b). These granites have relatively low MgO (0.70–1.13 wt%) contents with Mg# values of 41.13–44.08. They are metaluminous to weakly peraluminous, with A/CNK [molar $Al_2O_3/(CaO+Na_2O+K_2O)$] values ranging from 0.97 to 1.01 (Fig. 5c).

In contrast, the LJS quartz diorites are intermediate to acidic in composition with SiO_2 contents ranging from 61.17 to 65.31 wt% (Fig. 5a). They are high in Na_2O (4.53–4.94 wt%), yet low in K_2O (1.65–2.09 wt%), with K_2O/Na_2O weight ratios of 0.34–0.46, showing an affinity to calc-alkaline rocks (Fig. 5b). These quartz diorites are metaluminous, with A/CNK values of 0.85–0.96 (Fig. 5c). They have higher CaO (4.36–5.51 wt%), $Fe_2O_3^T$ (3.82–5.63 wt%), MgO (1.80–3.07 wt%), TiO_2 (0.45–0.57 wt%), and Mg# (48.09–51.93) compared to the HJS granites. All of the rocks from the HJS and LJS plutons have relatively low $FeO^T/(FeO^T+MgO)$ weight ratios (0.62–0.72), and fall within the magnesian-type granitoids field (Fig. 5d) according to the scheme of Frost et al. (2001).

All of the granite and quartz diorite samples have similar total rare earth element (∑REE) concentrations, ranging from 106–150 ppm and 116–218 ppm, respectively. They show similarly fractionated chondrite-normalized REE patterns and are marked by significant light REE (LREE) enrichment, HREE depletion, and negligible Eu anomaly (Fig. 6a) with consequently high $(La/Yb)_N$ of 13.82–19.00 and 21.29–42.76, respectively. These granitoids have primitive-mantle-normalized multi-element variation patterns that are enriched in the large ion lithophile elements (LILEs; e.g., Rb, Th, and U) and relatively depleted in the high field strength elements (HFSEs; e.g., Nb, Ta, Ti). They show a negative P anomaly (Fig. 6b). Despite these similarities, there are several differences in the compositions of the HJS granites and LJS quartz diorites. The LJS quartz diorites typically have more significant depletions in the HREE, Y, Ta, Nb, and Rb, greater enrichment in the Sr, Ni, Co, and Cr, and higher Sr/Y and La/Yb ratios compared to the HJS granites.

Whole-rock Rb–Sr and Sm–Nd isotopes

Whole-rock Sr–Nd isotopic compositions for the HJS granites and LJS quartz diorites are listed in Table 2. Both have similar initial $^{87}Sr/^{86}Sr$ values (I_{Sr}) of 0.7062–0.7063 and 0.7059–0.7061, respectively. Moreover, they have homogeneous Nd isotopic compositions with $\varepsilon_{Nd}(t)$ values ranging from

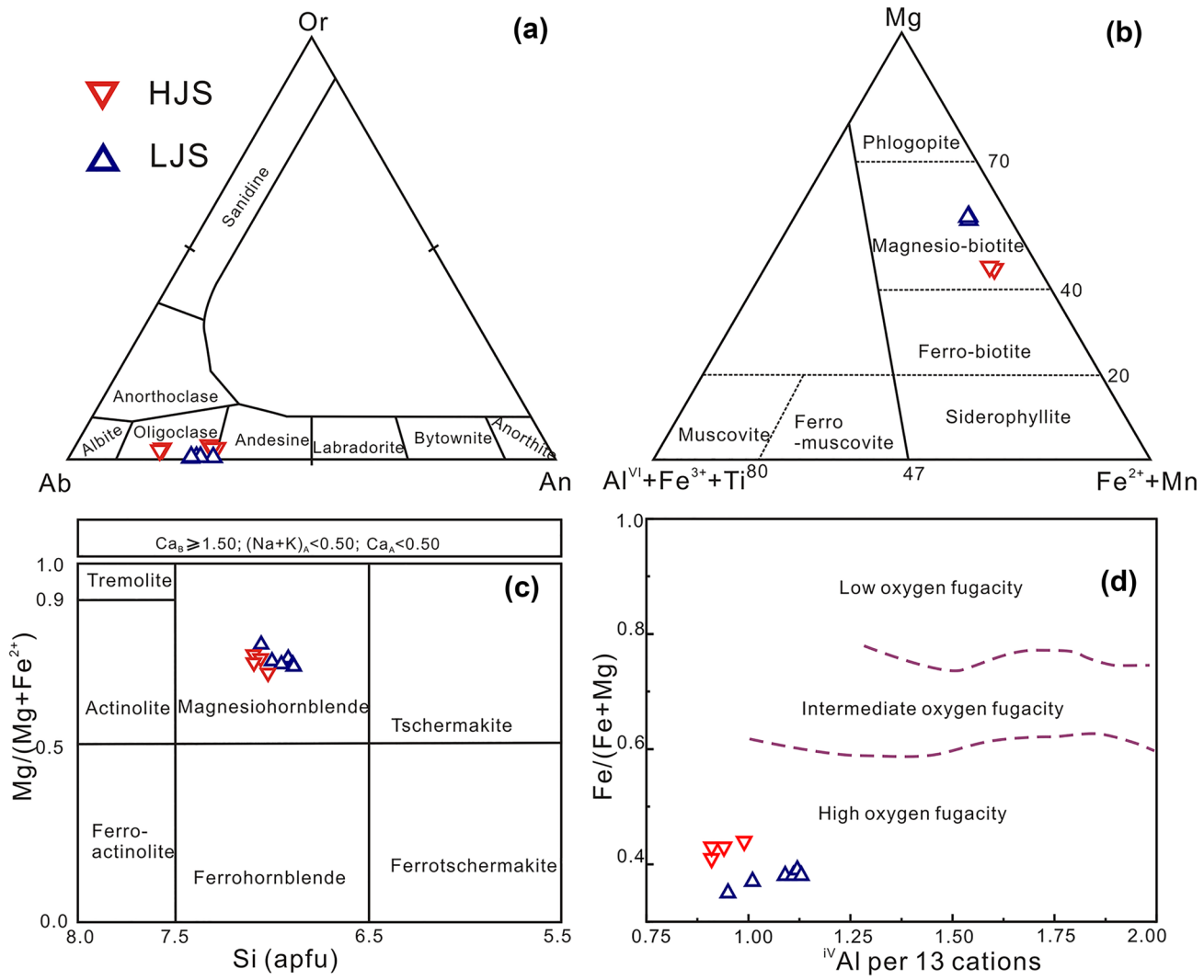

Fig. 4 (**a**) An-Or-Ab diagram for plagioclases (after Deer et al. 1992). (**b**) Classification diagram for biotite from the HJS and LJS granitoids (after Foster 1960). (**c**) Classification of amphiboles from the HJS and LJS granitoids (after Leake et al. 1997). (**d**) (Fe + Mg)] versus ^{iv}Al of the hornblendes from the HJS and LJS granitoids (fields after Anderson and Smith 1995), suggesting their formation under high oxygen fugacity

-0.37 to + 0.99 for the HJS granites and -0.65 to + 0.77 for the LJS quartz diorites (Fig. 7a). All of the samples have relatively young two-stage Nd model ages (T_{DM2}: 1.10–1.21 Ga for the HJS granites and 1.12–1.23 Ga for the LJS quartz diorites).

Zircon Hf isotopic compositions

The in-situ Hf isotopic compositions of the zircons from samples HJS-2 and LJS-1 are listed in Table S6 and plotted in Fig. 7b. For the calculation of $\varepsilon_{Hf}(t)$ and T_{DM2} values, we used the zircon U–Pb ages obtained in this study. Granitoids from the HJS and LJS plutons are characterized by relatively depleted and homogeneous zircon Hf isotopic compositions. Zircon grains from the sample HJS-2 show initial $^{176}Hf/^{177}Hf$ ratios of 0.282552–0.282648 and yield $\varepsilon_{Hf}(t)$ values ranging from + 2.0 to + 5.4, with two-stage Hf model ages (T_{DM2}) of 1.08–1.30 Ma. In contrast, the zircons from sample LJS-1 have greater radiogenic Hf isotope compositions compared to the HJS pluton, with initial $^{176}Hf/^{177}Hf$ ratios of 0.282643–0.282724, $\varepsilon_{Hf}(t)$ values of + 5.1 to + 8.0, and T_{DM2} model ages of 0.91–1.10 Ga.

Discussion

Petrogenesis

Origins of the HJS and LJS adakitic rocks

All samples from both the HJS and LJS plutons are characterized by relatively high Al_2O_3 (> 14 wt%),

Table 1 Major and trace element compositions of the HJS and LJS granitoids

Pluton	HJS					LJS					
Sample	HJS-1	HJS-2	HJS-3	HJS-4	HJS-5	LJS-1	LJS-2	LJS-3	LJS-4	LJS-5	LJS-6
Major contituents (wt%)											
SiO_2	71.43	70.00	69.32	69.80	69.54	63.14	60.17	63.04	63.70	65.31	62.84
TiO_2	0.30	0.22	0.25	0.32	0.35	0.48	0.57	0.48	0.47	0.45	0.49
Al_2O_3	14.96	13.74	15.05	14.75	14.53	17.17	16.76	17.21	17.12	16.67	16.84
$Fe_2O_3^T$	2.61	1.96	2.12	2.65	2.84	4.49	5.63	4.23	3.95	3.82	4.72
MnO	0.06	0.04	0.05	0.05	0.07	0.07	0.10	0.07	0.07	0.06	0.08
MgO	1.03	0.70	0.84	1.01	1.13	2.10	3.07	2.02	1.85	1.80	2.31
CaO	2.36	1.77	2.19	2.47	2.50	4.87	5.51	4.75	4.64	4.36	5.03
Na_2O	3.83	3.77	3.86	3.99	4.05	4.87	4.53	4.84	4.94	4.68	4.57
K_2O	3.89	4.14	4.31	3.76	3.40	1.67	2.09	1.69	1.75	1.65	1.71
P_2O_5	0.10	0.07	0.09	0.10	0.11	0.23	0.33	0.22	0.20	0.19	0.24
LOI	0.54	2.64	1.01	0.63	0.82	0.86	0.90	1.19	1.23	0.87	0.19
Total	101.10	99.05	99.08	99.53	99.32	99.96	99.64	99.75	99.92	99.85	99.01
$K_2O + Na_2O$	7.72	7.91	8.17	7.75	7.45	6.54	6.62	6.53	6.69	6.33	6.28
K_2O/Na_2O	1.02	1.10	1.12	0.94	0.84	0.34	0.46	0.35	0.35	0.35	0.37
A/CNK	1.01	0.99	1.00	0.97	0.97	0.92	0.85	0.93	0.93	0.96	0.91
Mg#	43.9	41.4	44.0	43.0	44.1	48.1	51.9	48.6	48.1	48.3	49.2
Trace elements (ppm)											
Sc	4.64	3.60	4.33	5.13	5.22	8.21	11.7	7.82	7.81	6.99	9.01
V	43.0	36.3	41.0	45.0	39.5	97.8	140.9	93.1	90.5	87.9	104
Cr	43.5	54.1	47.9	43.2	17.1	38.7	56.7	34.3	32.6	33.2	43.3
Co	6.14	4.24	5.06	6.69	6.86	14.8	20.4	13.8	11.8	12.0	15.4
Ni	10.3	5.69	6.83	9.27	8.01	18.1	26.9	16.6	14.0	14.8	21.1
Cs	5.57	4.35	3.84	4.94	5.51	3.10	3.70	3.11	2.74	2.34	3.88
Rb	120.8	159.6	135.9	129.2	129.8	44.4	62.5	34.3	31.4	32.5	34.4
Ba	814	579	1084	843	473	915	1194	773	960	960	774
Th	20.1	23.2	16.4	14.8	22.7	10.2	12.3	10.8	9.92	15.1	9.49
U	3.24	5.54	2.62	3.07	3.11	3.00	3.96	2.72	2.24	2.05	2.34
Ta	1.25	1.83	1.48	1.35	1.57	0.41	0.51	0.51	0.43	0.35	0.38
Nb	12.7	14.7	11.2	12.3	14.0	6.52	10.7	6.45	7.14	5.59	6.58
Pb	22.6	25.5	23.6	22.0	25.7	18.5	21.9	18.5	16.3	15.7	16.9
Sr	312	232	330	333	302	753	788	696	704	686	633
Nd	19.9	17.4	16.6	21.4	23.4	24.9	44.0	22.6	25.1	23.6	25.0
Zr	134.4	102.2	117.8	133.7	132.7	156.7	162.8	134.8	137.0	134.7	133.0
Hf	4.38	3.67	3.68	4.20	4.31	4.23	4.47	3.67	3.54	3.40	3.68
Sm	3.28	2.92	2.76	3.40	3.76	3.93	7.17	3.76	3.85	3.37	4.14
Ti	1774	1338	1615	1951	2097	2931	3516	2937	3065	2947	2949
La	27.6	28.4	24.7	34.5	37.4	32.3	45.4	26.7	35.3	39.5	29.8
Ce	58.4	47.7	48.2	60.9	67.2	58.1	92.9	47.2	57.1	59.4	48.4
Pr	5.69	5.11	4.83	6.28	6.84	6.73	11.43	5.91	6.88	6.81	6.60
Nd	19.9	17.4	16.6	21.4	23.4	24.9	44.0	22.6	25.1	23.6	25.0
Sm	3.28	2.92	2.76	3.40	3.76	3.93	7.17	3.76	3.85	3.37	4.14
Eu	1.03	0.77	0.95	1.06	0.87	1.35	2.06	1.26	1.17	1.05	1.30
Gd	3.40	2.97	2.47	3.52	3.80	3.90	6.79	3.48	3.14	2.83	3.99
Tb	0.42	0.40	0.34	0.43	0.48	0.44	0.78	0.42	0.39	0.34	0.47
Dy	2.12	2.08	1.83	2.08	2.34	1.90	3.34	1.87	1.83	1.54	2.10
Ho	0.40	0.40	0.35	0.39	0.44	0.33	0.58	0.33	0.32	0.27	0.37
Er	1.25	1.27	1.06	1.23	1.38	1.00	1.73	0.98	0.92	0.79	1.10
Tm	0.18	0.19	0.16	0.18	0.20	0.12	0.22	0.12	0.12	0.10	0.14

Table 1 (continued)

Pluton	HJS					LJS					
Yb	1.29	1.38	1.10	1.22	1.40	0.82	1.44	0.81	0.76	0.62	0.91
Lu	0.21	0.22	0.18	0.20	0.22	0.13	0.22	0.13	0.12	0.10	0.14
Y	11.2	11.7	10.2	11.2	12.5	8.82	15.4	8.85	9.14	7.63	9.74

LOI loss on ignition, *A/CNK* $Al_2O_3/(CaO+Na_2O+K_2O)$ molar, *Mg#* [=100 × Mg/(Mg + Fe)], $Fe_2O_3^T$– total Fe expressed as Fe_2O_3

Sr (232–788 ppm), low Y (< 18 ppm), and Yb (0.62–1.44 ppm) contents, and corresponding high Sr/Y and La/Yb ratios. All samples fall in the adakite field on the Sr/Y versus Y and $(La/Yb)_N$ versus $(Yb)_N$ plots (Fig. 8a and b). They have low HREE concentrations and strongly fractionated REE patterns, with weak or no Eu anomalies. These geochemical features are comparable to those of adakite (Castillo 2012; Defant and Drummond 1990). Given that the HJS and LJS plutons have similar Sr–Nd isotopic compositions and zircon U–Pb ages, it

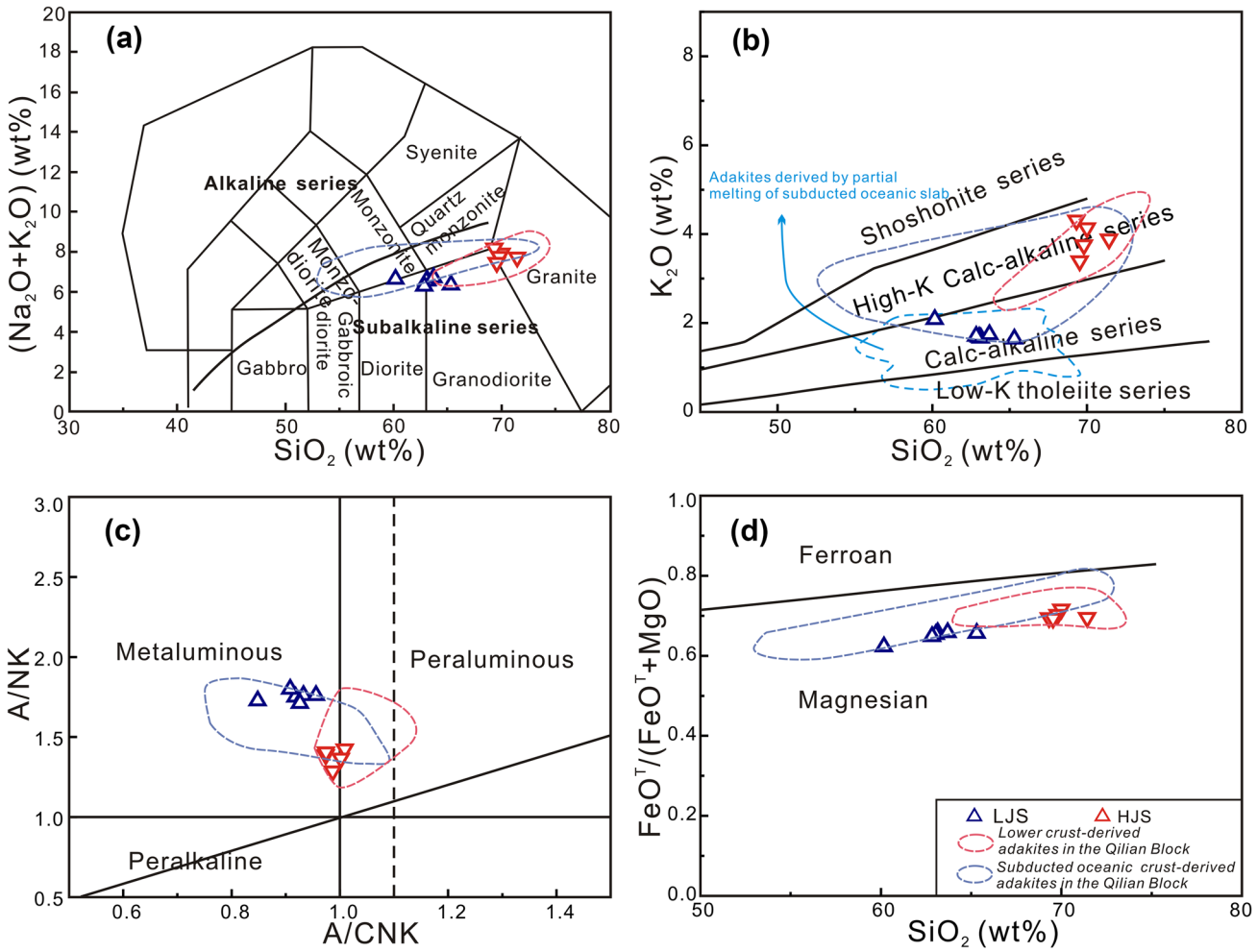

Fig. 5 Chemical classification of granitoidic rocks from the HJS and LJS plutons, NW China. (**a**) Total alkali versus silica (TAS) diagram (Middlemost 1994; with the thick solid line from Irvine and Baragar 1971); (**b**) K_2O versus SiO_2 plot (Peccerillo and Taylor 1976); (**c**) A/NK versus A/CNK diagram (Chappell and White 1974; Maniar and Piccoli 1989); (**d**) $FeO^T/(FeO^T+MgO)$ versus SiO_2 plot (after Frost et al. 2001). Data sources: Eary Paleozoic lower crust-derived adakites in the Qilian Block (Tung et al. 2016; Yang et al. 2015, 2016), Early Paleozoic subducted oceanic crust-derived adakites in the Qilian Block (Yang et al. 2015). The field of slab-derived adakites is after Wang et al. (2006b)

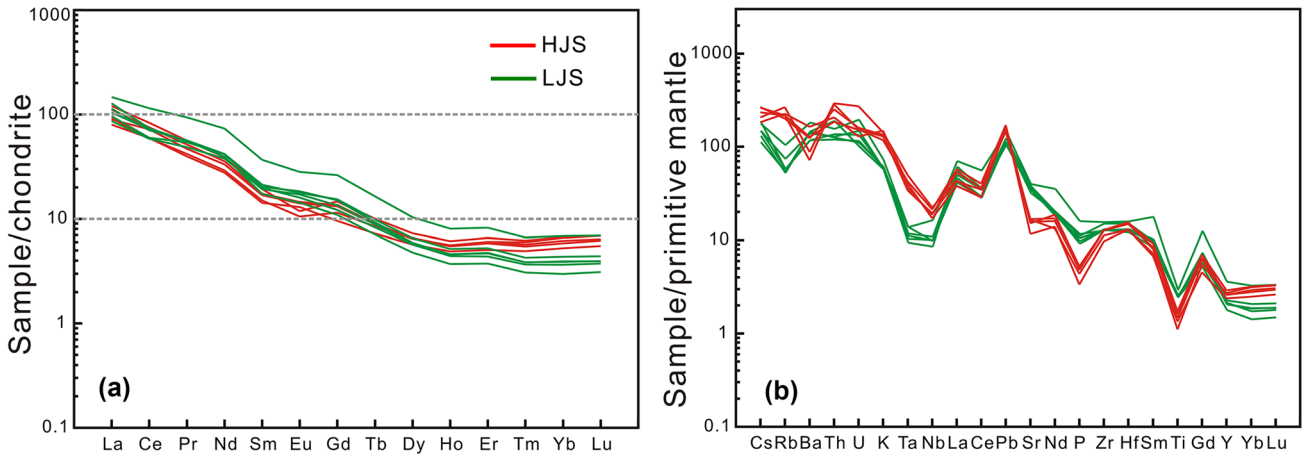

Fig. 6 Chondrite-normalized REE patterns (**a**) and primitive-mantle-normalized trace element spiderdiagrams (**b**) for rocks from the HJS and LJS plutons. The normalization values for chondrite and primitive mantle are from Boynton (1984) and McDonough and Sun (1995), respectively

appears that they were co-magmatic. However, distinct differences in major and trace elements and zircon Hf isotopic compositions indicate that their parental melts were derived from different sources (Figs. 5 and 6).

It has been suggested that fractionation of garnet and amphibole could yield similar geochemical features to those of adakites because of their preferential incorporation of HREEs over LREEs (Moyen 2009 and references therein). The LJS quartz diorites (440 Ma) were emplaced significantly later than the mafic rocks within the Lajishan area (ca. 525–470 Myr ago, Fu et al. 2014, 2017; Yan et al. 2015; Zhang et al. 2017), and also have much lower $\varepsilon_{Nd}(t)$ values (-0.65 – + 0.77) than those of the mafic rocks ($\varepsilon_{Nd}(t) = +4.83 - +6.34$, Fu et al. 2017). Both the HJS and LJS adakitic rocks display almost constant Dy/Yb ratios with increasing SiO_2 contents, suggesting insignificant fractionations of amphibole and garnet (Fig. 8c). Moreover, they have high Al_2O_3 contents and do not exhibit any conspicuous negative Sr and Eu anomalies (Fig. 6), which is inconsistent with the significant fractional of plagioclase. Therefore, the possibility of low-pressure or high-pressure fractional crystallization of basaltic melts for the origin of the HJS and LJS granitoids does not seem feasible.

Adakitic rocks formed by magma mixing usually have extremely high MgO (mostly > 3 wt%), Ni and Cr concentrations, and Mg# values (mostly > 52) (Chen et al. 2013; Streck et al. 2007), inconsistent with those observed in the HJS and LJS plutons. Both of the adakitic plutons show limited variations in whole-rock Sr–Nd and zircon Hf isotopic compositions (Fig. 7), suggesting that magma mixing between felsic and basaltic magmas is not a reasonable hypothesis for the generation of the adakitic granitoids in this study. This is further supported by the absence of petrographic disequilibrium textures in the LJS and HJS granitoids (Fig. 2), which is generally considered to be crucial petrographic evidence for mixing between basaltic and felsic magmas (Chen et al. 2013; Wang et al. 2019).

Adakite derived from partial melting of a subducted oceanic slab is typically enriched in Na and contains high $CaO + Na_2O$ contents, moderately high SiO_2, and low

Table 2 Whole-rock Rb–Sr and Sm–Nd isotopic data for the HJS and LJS granitoids

Sample no	t (Ma)	Rb (ppm)	Sr (ppm)	$^{87}Rb/^{86}Sr$	$^{87}Sr/^{86}Sr$	$(^{87}Sr/^{86}Sr)_i$	Sm (ppm)	Nd (ppm)	$^{147}Sm/^{144}Nd$	$^{143}Nd/^{144}Nd$	$\varepsilon_{Nd}(t)$	T_{DM2} (Ga)
HJS-2	445	159.6	232.1	1.9908	0.718955 ± 7	0.7063	2.92	17.4	0.1014	0.512341 ± 8	-0.37	1.21
HJS-4	445	129.2	333.1	1.1222	0.713374 ± 8	0.7062	3.40	21.4	0.0960	0.512395 ± 5	0.99	1.10
LJS-1	440	44.5	753.0	0.1707	0.706975 ± 7	0.7059	3.93	24.9	0.0954	0.512317 ± 4	-0.56	1.22
LJS-3	440	34.3	696.1	0.1424	0.707029 ± 7	0.7061	3.76	22.6	0.1004	0.512397 ± 5	0.70	1.12

$\varepsilon_{Nd}(t)$ values are calculated by granitoid ages and based on ^{147}Sm decay constant of 6.54×10^{-12}, the $^{143}Nd/^{144}Nd$ and $^{147}Sm/^{144}Nd$ ratios of chondrite and depleted mantle at present day are 0.512630 and 0.1960, 0.513151 and 0.2136, respectively (Miller and O'Nions 1985). T_{DM2} ages are calculated according to the two-stage model as presented by Wu et al. (2002)

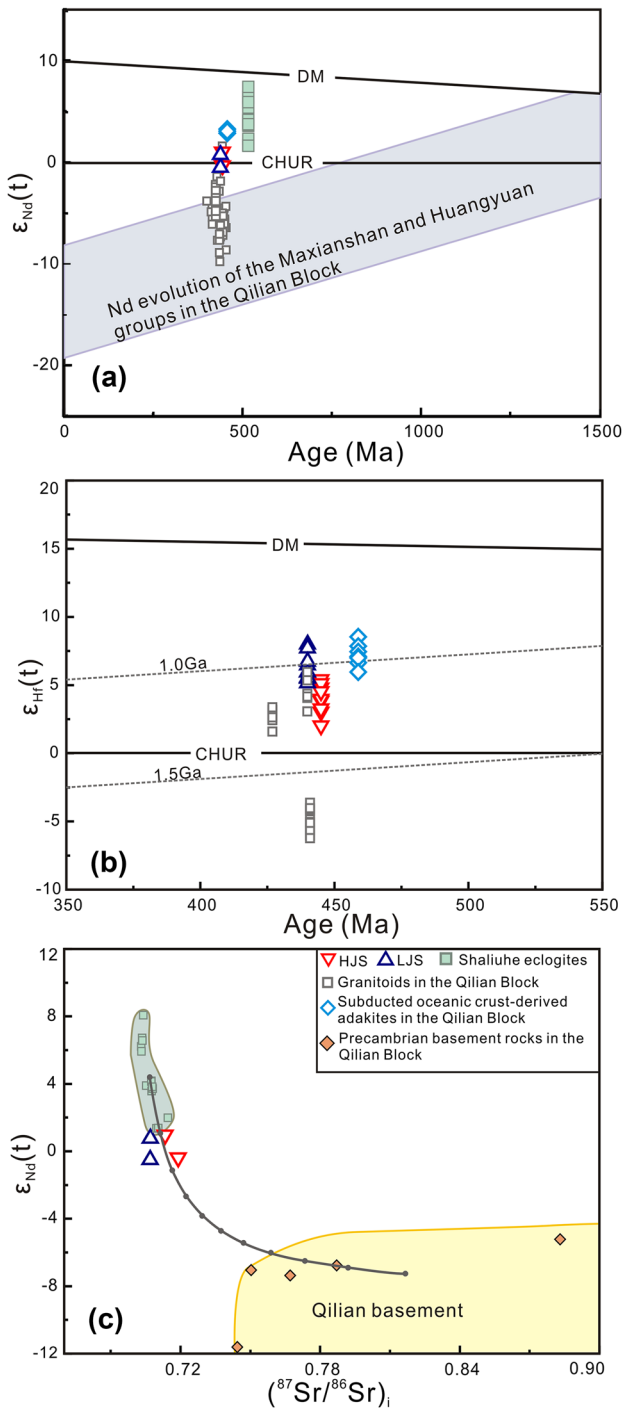

Fig. 7 (**a**) εNd(t) versus age plot for samples from the HJS and LJS plutons. DM, depleted mantle; CHUR, chondritic uniform reservoir. The Nd evolutionary area shown for the basement rocks of the Maxianshan and Huangyuan Groups in the Qilian Block is calculated by the data from Zhang et al. (2006). (**b**) Zircon $\varepsilon_{Hf}(t)$ versus age plot for the HJS granite and LJS quartz diorite. (**c**) $(^{87}Sr/^{86}Sr)_i$ versus $\varepsilon_{Nd}(t)$ plot for the HJS and LJS granitoids, all the isotopic data were calculated for t = 445 Ma. The black line represents the calculated binary mixing between the South Qilian Ocean MORB and terrestrial sediments (Precambrian basement in Qilian Block). The Qilian basement is represented by the Precambrian parametamorphic rock of Hualong group. The Shaliuhe eclogite is used to represent the ocean crust. Data sources: Eary Paleozoic granitoids in the Qilian Block (Tung et al. 2016; Yang et al. 2015, 2016), the Shaliuhe eclogite (Zhang et al. 2008), the Qilian basement (Xu, 2007)

K_2O with K_2O/Na_2O weight ratios of ~ 0.4 (Defant and Drummond 1990; Martin 1999). The LJS quartz diorites are characterized by high Na_2O (4.53–4.94 wt%) and $CaO + Na_2O$, low to medium K_2O (1.65–2.09 wt%) contents with K_2O/Na_2O weight ratios of 0.34–0.46, similar to those of adakite derived from basaltic oceanic crust (Fig. 5b). Moreover, the LJS quartz diorites have highly depleted zircon Hf isotopic compositions ($\varepsilon_{Hf}(t)$ values = + 5.1 to + 8.0), consistent with the magma derived from partial melting of oceanic crust. Althought most samples from the LJS pluton display medium MgO and Mg# and plot in the overlapping area of adakitic rocks derived from melting of subducting oceanic crust and lower continental crust in the Mg# and MgO discrimination diagrams (Figs. 8d and e), it should be noted that one adakitic samples from this pluton has significantly higher MgO (3.07 wt%) and Mg# (51.9) compared with those of the lower crust-derived melts (Figs. 8d and e). This further suggests that the LJS adakites had suffered interaction between the slab-derived adakitic melts and the overlying mantle peridotite during magma ascension (Li et al. 2016; Sen and Dunn 1994). In contrast, the HJS granites have relatively higher SiO_2, and LILEs (e.g., Rb, Cs, Th, and U), and lower Mg#, and Ce/Pb values, and MgO and compatible element contents (e.g., Ni and Co) compared to those of the LJS quartz diorites. The HJS granites are also enriched in K (K_2O = 3.40–4.31 wt%) with K_2O/Na_2O weight ratios of 0.84–1.12. These geochemical features are similar to those of lower continental crust-derived adakitic rocks found in the eastern Qilian Block and Dabie Orogen (Wang et al. 2007a; Yang et al. 2015) and are distinctly different from slab-derived adakites or delaminated lower continental crust-derived adakitic rocks, which usually display high MgO, Cr, Ni, and Co concentrations and high Mg# values because of interaction with a mantle source (Gao et al. 2004; Xu et al. 2002).

Experimental studies show that melts produced by partial melting of low-K MORB compositions at pressures of 1 to 2 GPa and temperatures < 1100 °C are generally characterized by high Al_2O_3 and Na_2O contents, and low K_2O/Na_2O weight ratios (Prouteau et al. 2001; Sen and Dunn 1994), whereas those derived by partial melting of a thickened lower crustal source (metabasaltic or eclogitic material) typically have relatively low MgO concentrations (< 3 wt%) and Mg# values (< 50), and relatively high K_2O concentrations (Rapp et al. 2002; Wang et al. 2007a). In the SiO_2 versus MgO and Al_2O_3 versus K_2O/Na_2O plots (Fig. 8), samples from the HJS pluton plot in the field of adakitic rocks derived from partial melting of a thickened lower crust and the LJS pluton in the subducted oceanic crust field. In addition, the LJS granitoids have higher CaO/Al_2O_3 weight ratios (0.26–0.33) compared to the HJS granites (0.13–0.17), similar to adakitic rocks formed by partial melting of subducted oceanic crust (CaO/

$Al_2O_3 > 0.2$, Li et al. 2016 and references therein). Furthermore, the ratios between LILEs and HFSEs (e.g., Th/Nb and Th/Zr) are significantly lower in the LJS granitoids than in the HJS granites. This coincides with our hypothesis (Fig. 9a and b), because LILEs are generally more incompatible than the HFSEs during crustal melting, and are relatively depleted in subducted oceanic crust melts due to dehydration prior to partial melting (Barboni and Bussy 2013; Hawkesworth et al. 1997; Zhao and Zhou 2007). Therefore, it is suggested that the HJS granites originated from the lower continental crust, and the LJS quartz diorites were principally generated from oceanic crust.

Whole-rock Sr–Nd isotope compositions of the LJS quartz diorites are slightly more enriched compared to the Shaliuhe eclogites derived from the MORB protolith in the NQ-UHPM belt (Fig. 7a) and the mafic rocks from the Lajishan area ($\varepsilon_{Nd}(t) = +4.83 - +6.34$, Fu et al. 2017). It is well accepted that the partial melting of slabs is usually accompanied by the melting of the overlying sediments (Castillo 2012; Tatsumi and Hanyu 2003; Wang et al. 2007b). On the SiO_2 versus Th/Yb plot, the LJS quartz diorites exhibit a well-defined positive correlation (Fig. 9c). Moreover, they have low to medium K_2O, high Ba, Th, and Th/Ce, significantly negative Nb–Ta-Ti anomalies, and a slightly positive anomaly of Eu. These geochemical characteristics are typical of oceanic sedimentary materials, further suggesting the inclusion of subducted sediments during the formation of the LJS quartz diorites (Benito et al. 1999; Woodhead et al. 2001). The most suitable source for the LJS pluton of the parental andesitic magmas with inherited mantle isotopic signatures thus is subducted oceanic crust with minor included subducted terrigenous sediments. Simple binary isotopic mixing modelling further suggests that the source of the LJS pluton was ~ 90% ocean crust and ~ 10% continental materials (Fig. 7c).

The HJS granites have relatively depleted zircon Hf isotopic compositions ($\varepsilon_{Hf}(t) = +2.0$ to $+5.4$). Their Nd isotope compositions are more depleted than those of the basement rocks from the Maxianshan group in the Lanzhou area (Fig. 7a), suggesting that they were not directly sourced through partial melting of thickened ancient basement rocks. The simple magma mixing model also has been excluded as the potential source, as discussed above. Moreover, the HJS granites have relatively young two-stage Nd-Hf model ages, which is inconsistent with any of the known episodes of regional crust generation (2.2–2.8 Ga and 1.60–1.85 Ga) proposed by Tung et al. (2012, 2013, 2016). This indicates that a basaltic lower crust source for the HJS pluton would be juvenile, most likely from a mixed lithology formed by pre-existing lower crust underplated by mantle-derived mafic magma.

Overall, we conclude that the calc-alkaline LJS adakitic quartz diorite was formed by partial melting of subducted oceanic crust with the addition of minor oceanic sedimentary material. In contrast, the high-K calc-alkaline HJS adakitic granite was most likely derived by partial melting of a thickened juvenile mafic lower crust.

Physical and chemical conditions for the HJS and LJS plutons

Ratios of middle REE (MREE) and HREE are generally sensitive to melting/fractionation pressures in magmas because the stability field of garnet contracts with decreasing pressure. In contrast, plagioclase stability generally positively correlates with magma water contents, yet is inversely related to pressure. The HJS granites show moderately heavy REE depletion. However, they have a flat, heavy REE pattern with $(Dy/Yb)_N$ values of 0.98–1.10, suggesting that the amphibole is the dominant residual mineral phase in the magma source and no significant garnet presence. In contrast, the LJS pluton shows significantly higher $(Sm/Yb)_N$, $(Dy/Yb)_N$, $(Ho/Yb)_N$, Y/Yb values and Sr concentrations, and lower Yb and Y contents than those of the HJS granites, suggesting the occurrence of residual garnet. On the $(La/Yb)_N$ versus $(Yb)_N$ plot, the LJS quartz diorites plot along the partial melting lines of 10% garnet-amphibolite, whereas the HJS granites plot between the partial melting lines of 10% garnet-amphibolite and amphibolite (Fig. 8b). This supports the idea that residual garnet played an essential role in the origin of LJS quartz diorites. In addition, the Nb/Ta ratios have been proven to be the most sensitive pressure proxy, as this elemental pair is strongly controlled by the presence of rutile rather than garnet and amphibole in the residue (Foley et al. 2002; Nagel et al. 2012). Partial melting of eclogites in the rutile stability field would yield melts with high Nb/Ta ratios because the rutile distribution coefficient of Ta is significantly greater than that of Nb (Foley et al. 2002). The Nb/Ta ratios of the LJS pluton (12.6–21.2) are significantly higher than the HJS pluton, further implying that rutile is a residual mineral in the source. This inference is supported by their negative Nb and Ta anomalies, low Nb/La ratios, and TiO_2-undersaturated characteristics, as shown in Figs. 6b and 9d. Therefore, the magma source for the HJS granites may not be as deep as that of typical adakites, with melting occurring at pressures less than 1.2 Gpa (Moyen and Stevens 2006), whereas the parental magma of the LJS pluton may have been produced at pressures higher than ~ 1.5 Gpa (Xiong et al. 2005). This is consistent with origins from a thickened juvenile mafic lower crust and a subducted oceanic crust, respectively.

The HJS granites have relatively low CaO content and $(CaO + Na_2O)/K_2O$ weight ratios, and weak depletion in Sr, as shown in Fig. 6. More importantly, their Sr contents range from 232 to 333 ppm, significantly lower than what is expected for typical adakites (> 400 ppm), indicating minor residual plagioclase in the magma source because of the low solubility

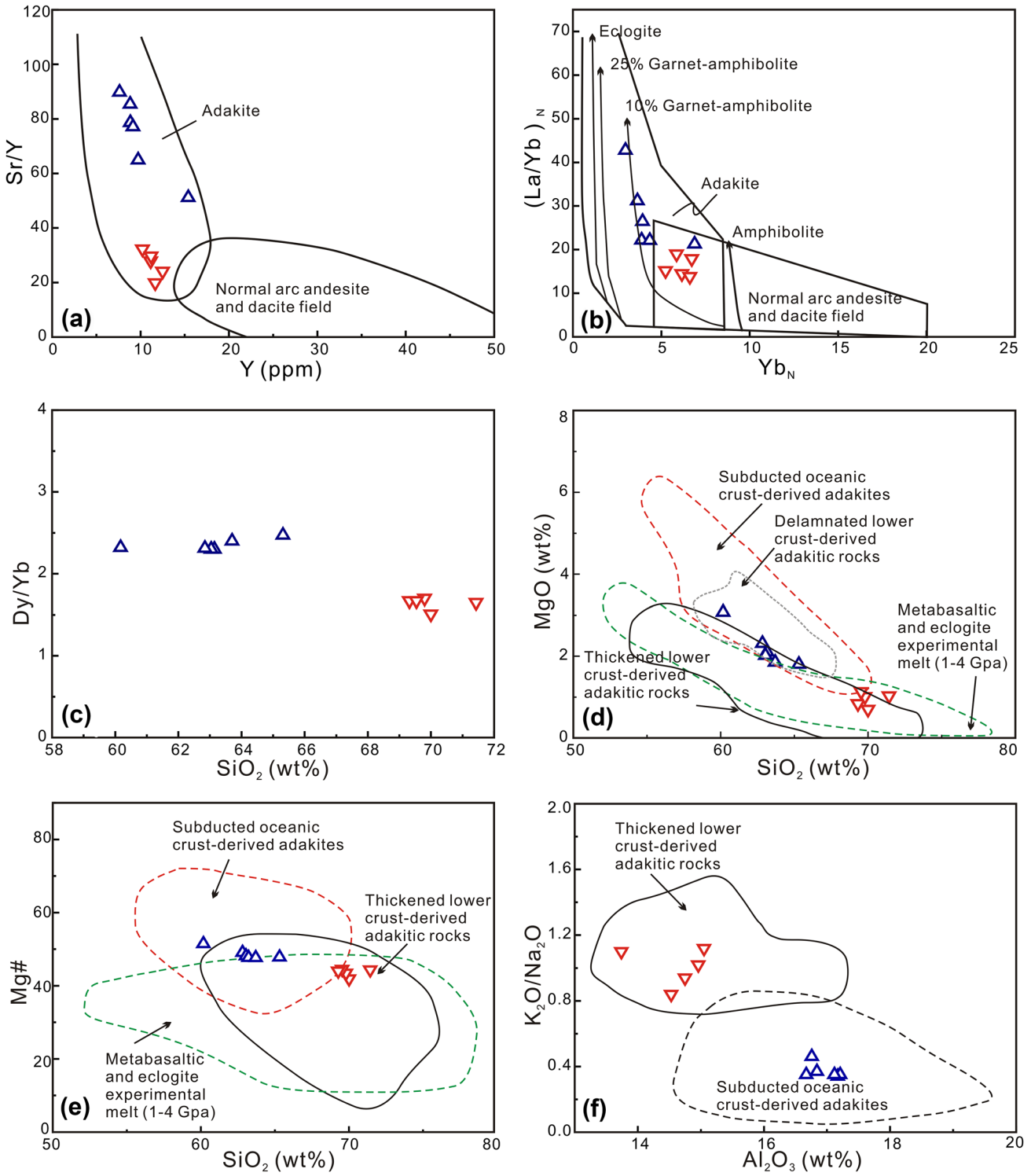

Fig. 8 (**a**) Sr/Y versus Y plot (after Defant and Drummond 1990); (**b**) $(La/Yb)_N$ versus Yb_N plot (after Drummond and Defant 1990); (**c**) SiO_2 versus Dy/Yb plot; (**d**) MgO versus SiO_2 plot, fields for different types of adakite and data sources are taken from Wang et al. (2006a, b); (**e**) MgO versus SiO_2 plot (after Wang et al. 2012); (**f**) K_2O/Na_2O versus Al_2O_3 plot (after Liu et al. 2010a, b). Same symbols as in Fig. 4

of plagioclase (Conrad et al. 1988) and relatively low melting pressure. In contrast, the high Al_2O_3 and Sr contents, and mostly positive Eu anomalies of the LJS quartz diorites suggest retarded crystallization of plagioclase, which, when coupled with the abundant amphibole as well as biotite and titanite in the rocks, indicate an origin from an H_2O-rich magma (Conrad et al. 1988; Richards 2011). Ridolfi et al. (2010) mentioned that ^{vi}Al in amphibole is sensitive to the water content of the melt, and proposed a hygrometric formula to estimate the H_2O content in the melt ($H_2O_{melt} = 5.215\,^{vi}Al^* + 12.28$). The estimated water contents in the LJS pluton would have been 1.5–2.4 wt% and 0.35–1.07 wt% for the HJS pluton based on this formula. This also is evidence that the LJS pluton had a much higher water content than those of the HJS pluton. Additionally, both the HJS and LJS granitoids commonly belong to magnesian-subtype according to the scheme of Frost et al. (2001) based on the consideration of their high $FeO^T/(FeO^T + MgO)$ values. Elevated whole-rock V/Sc and V/Co, and low $Fe^{total}/(Fe^{total} + Mg)$ but high $Fe^{3+}/(Fe^{2+} + Fe^{3+})$ ratios in the amphiboles are observed in both granitoids (Fig. 4d). These indicate their formation in a relatively oxidizing condition, consistent with relatively high magnetite contents and the occurrence of titanite in the LJS pluton (Anderson and Smith 1995; Foley and Wheller 1990; Frost et al. 2001; Li et al. 2012; Papoutsa and Pe-Piper 2014; Zhu et al. 2014). Collectively, we conclude that both were produced in a relatively oxidized environment, and the parental magma of the LJS rocks was more water-rich than those for the HJS granites.

Tectonic implications for the northward subduction of the South Qilian Ocean Plate

The Qilian Block, located between the North Qilian Orogenic Belt and NQ-UHPM belt, is predominantly Precambrian

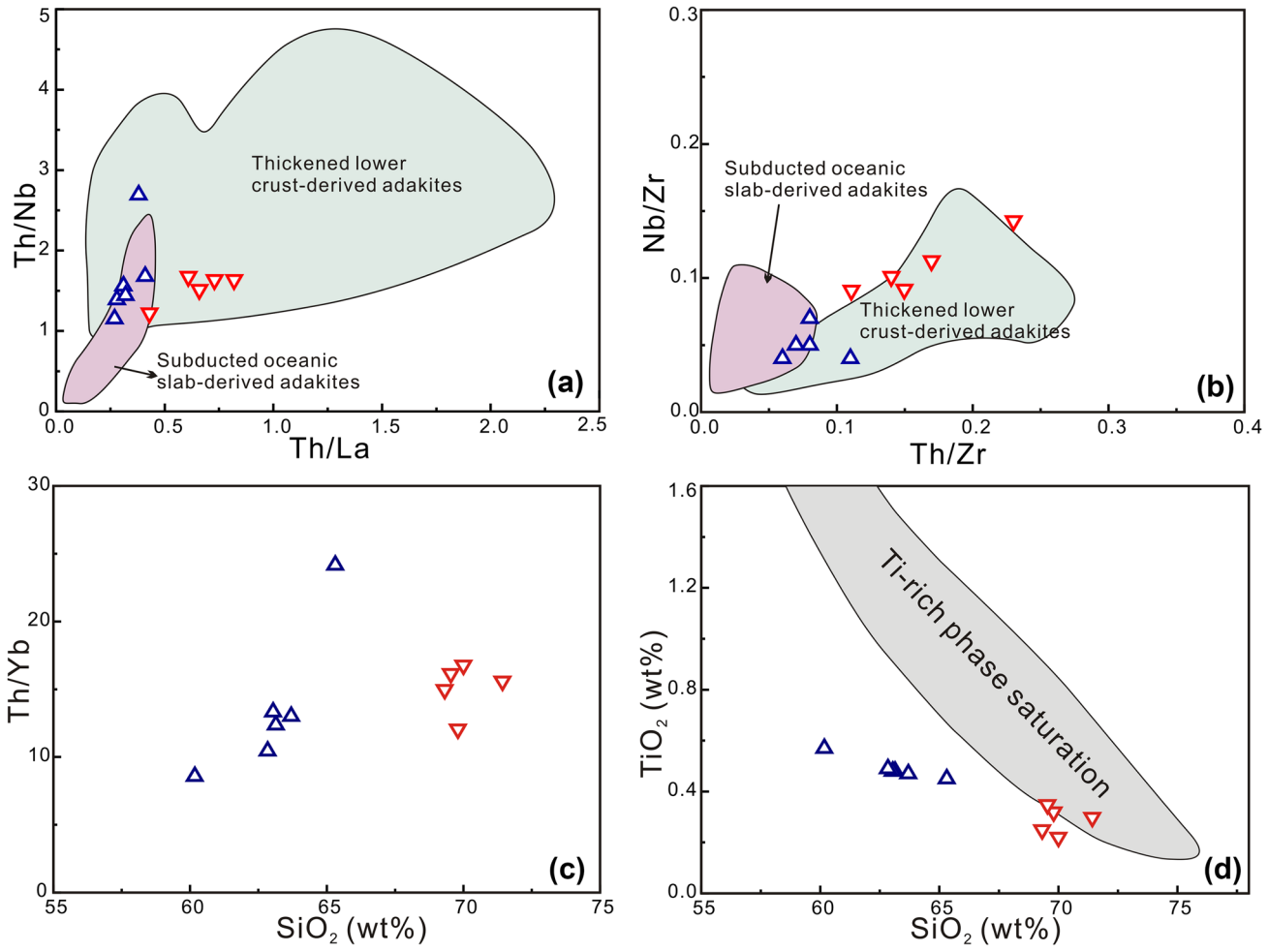

Fig. 9 (**a**) Th/La versus Th/Nb plot; (**b**) Th/Zr versus Nb/Zr plot; (**c**) SiO_2 versus Th/Yb plot; and (**d**) SiO_2 versus TiO_2 plot. The fields for adakites generated from subducted oceanic slab and thickened crust are from Stern and Kilian (1996) and Wang et al. (2006b), respectively. TiO_2 saturation field for the melt derived from partial melting of basic rocks is from Xiong et al. (2011). Same symbols as in Fig. 4

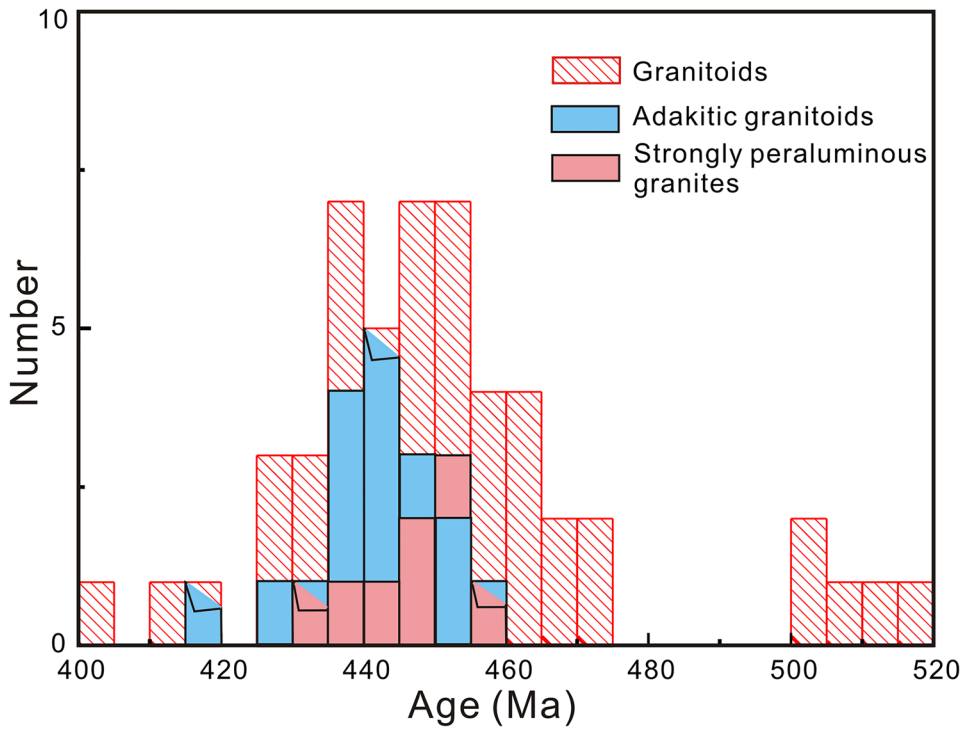

Fig. 10 Frequency of zircon U–Pb ages for the magmatic rocks from the eastern Qilian Block. Data are from Table S1

basement and is characterized by widespread and voluminous Early Paleozoic granitoids with minor basaltic rocks (Gao et al. 2018; Li et al. 2018; Tung et al. 2016; Xia et al. 2016; Yang et al. 2015, 2016). The geodynamic mechanism responsible for the generation of the Early Paleozoic magmatism within the Qilian Block still remains controversial. Two main tectonic models have been proposed to explain the tectonic evolutionary process of the Qilian orogeny during the Early Paleozoic (see details in the Introduction, Huang et al. 2015; Li et al. 2017; Tung et al. 2016; Yang et al. 2015, 2016). These models debate the location of the suture zone and the subduction polarity of the oceanic lithosphere (Huang et al. 2015; Li et al. 2017; Song et al. 2014a, b; Tung et al. 2016; Xia et al. 2016; Yang et al. 2015, 2016).

The occurrence and stability of abundant euhedral hornblende and biotite, as well as magnetite crystals in the LJS and HJS plutons, indicate oxidized and water-rich conditions, which relate to their derivation with plate subduction processes (Richards 2015). Several Cambrian granitoidic plutons along the northern margin of the Qilian Block are recognized, including the Kekeli (ca. 512 Ma, Wu et al. 2010), Menyuan (ca. 505–500 Ma, Huang et al. 2015; Peng et al. 2017), and Xiagucheng (ca. 505 Ma, Qin et al. 2014) plutons, supporting southward subduction of the North Qilian Ocean during the Late Cambrian. However, the southward subduction of the North Qilian Ocean is difficult to explain the formation of ca. 517 Ma quartz diorite and ca. 505–493 Ma gabbros in the Lajishan region in the southern part of the Qilian Block (Cui et al. 2018; Tao et al. 2018; Yang et al. 2021). In addition, a compilation of available geochronological data for the igneous rocks within the eastern part of the Qilian Block suggests that Early Paleozoic magmatism mainly occurred in the range from 464 to 402 Myr ago, with a major peak between 455 and 435 Myr ago (Fig. 10). Only minor Cambrian–Middle Ordovician (ca. 517–464 Ma) magmatic rocks are exposed in the Qilian Block, and those with ages of ca. 500–464 Ma are predominantly distributed in the Lajishan region (Cui et al. 2018; Tao et al. 2018; Yang et al. 2021). There appears to have been a magmatic hiatus in the range from 500 to 464 Myr ago in the northern margin of the Qilian Block (Fig. 1a). Moreover, the North Qilian Orogenic Belt developed a characteristic trench–arc–basin system during the Early Paleozoic, and the corresponding voluminous widespread magmatism was essentially continuous from 516 to 402 Myr ago (Song et al. 2013; Xia et al. 2016). These suggest that the subduction polarity for the North Qilian oceanic basin during the Early Paleozoic was dominantly northwards, and its southwards subduction only occurred during the initial stage of slab subduction. The ca. 464–402 Myr ago magmatism in the Qilian Block thus could not be related to the southwards subduction of the North Qilian oceanic plate. Temporal and spatial variations of the magmatic rocks in the Qilian Block thus clearly suggest the northward subduction of the Early Paleozoic oceanic lithosphere existed in the south of the Qilian Block. Identifications of ophiolite sequences and island arc volcanic rocks (514 Ma, Shi et al. 2006; Zhang et al. 2008) in the NQ-UHPM belt imply that an ocean

existed between the Qilian Block and Qaidam-West Qinling Orogenic belt (namely, the South Qilian Ocean). Xu et al. (2006) and Li et al. (2018) confirmed the existence of this ocean and further suggested that it occurred as a branch of the proto-Tethys ocean after the breakup of the Rodinia supercontinent. Moreover, the WNW–ESE-trending NQ-UHPM belt is considered to have resulted from the ca. 495–440 Myr ago deep subduction of the South Qilian Ocean and the Qaidam continental crust beneath the Qilian Block (Xu et al. 2006). Taken together, it is suggested that there was an Early Paleozoic ocean basin (South Qilian Ocean) located between Qilian and Qaidam Blocks, and the northward subduction of this oceanic lithosphere beneath the Qilian Block, and the subsequent continental collision are the main mechanisms responsible for the development of the Early Paleozoic voluminous intense magmatism within the Qilian Block.

Zircon U–Pb dating indicates that the HJS and LJS granitoids in this study were emplaced between 445 and 438 Myr ago. Combined with previous studies, this suggests that adakitic magmatism in the Qilian Block occurred over a relatively long, protracted period (from ca. 459 to 419 Myr ago), peaking at ~ 445 Ma (Table S1; Fig. 10). Similarly, strongly peraluminous granites from the Qilian Block have concentrated ages in the range from ca. 455 to 431 Ma, peaking at ~ 450 Ma (Fig. 10). This suggests a significantly high heat flux in the Qilian Block during the Late Ordovician–Early Silurian (Barbarin 1999; Liégeois 1998). Moreover, several ca. 449–438 Ma gabbros within the Qilian Block closely coexist with coeval granitoids, such as the Heishishan, Bamishan, and Lumanshan plutons (Guo et al. 2015; Yang et al. 2015), and both them thus constitute a bimodal intrusive rock associations. Furthermore, there are numerous mafic dikes in the Maxianshan group (ca. 441–434 Myr ago, He et al. 2008) and small mafic–ultramafic dike-like intrusions along the southern margin of the Qilian Block (ca. 455–440 Myr ago, Yan et al. 2015; Yu et al. 2012; Zhang et al. 2014, 2015). These strongly suggest that the Qilian Block was in an extensional setting from ca. 455 to 434 Myr ago. This is further supported by the identification of the ca. 446 Ma Yindonggou A-type granitoid in the Qilian Block (Cui et al., 2018). All of these gabbros, basaltic dikes, and small mafic–ultramafic dike-like intrusions in the Qilian Block are geochemically enriched in LREEs and LILEs, and depleted in HFSEs, indicating their generation in a subduction-related environment. Therefore, the Late Ordovician–Early Silurian magmatism in the Qilian Block most likely occurred in a subduction-related extensional tectonic setting.

Both break-off and rollback of the subducted south Qilian oceanic slab have been proposed to explain the Early Paleozoic extensional setting in Qilian Block, NW China (Huang et al. 2015; Xia et al. 2016). The Early Paleozoic exhumation of the combined ultrahigh-pressure-metamorphosed oceanic and continental crust recorded in the North Qaidam ultra-high pressure metamorphic belt precludes the model of slab rollback during subduction. Notably, the LJS granitoids in this study show relatively high Mg# values and depleted Sr–Nd-Hf isotopic characteristics, and can be interpreted as the products of partial melting of the subducted ocean crust. This, coupled with the Liancheng, Gangcha and Bamishan high-Mg dioritic rocks (Tung et al. 2016) constitutes the igneous rock associations related to slab break-off (Ma et al. 2015a). Moreover, the ca. 460–435 Ma granitoids show a wide range of A/CNK, Mg#, and $\varepsilon_{Nd}(t)$ values (Figs. 7a and 11), suggesting that a large volume of mantle materials were added in a short period in response to slab break-off. Therefore, it is suggested that both the LJS and HJS adakitic rocks were probably generated in an extensional tectonic setting related to the break-off of the northward subducting South Qilian Ocean slab.

Accordingly, we suggest a simplified genetic model for the HJS and LJS granitoids in the eastern Qilian Block (Fig. 12). A deficiency of large-scale magmatism before 470 Ma in the

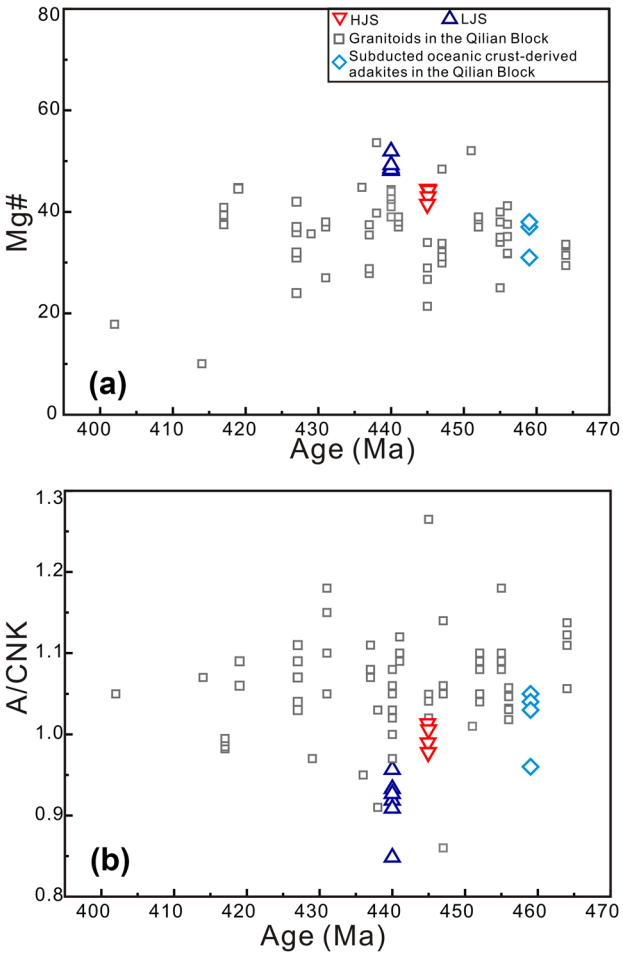

Fig. 11 Plots of Mg# (**a**) and A/CNK (**b**) versus ages for the Early Paleozoic granitoids in the eastern Qilian Block. Data sources for the Early Paleozoic granitoids in the eastern Qilian Block as in Fig. 7

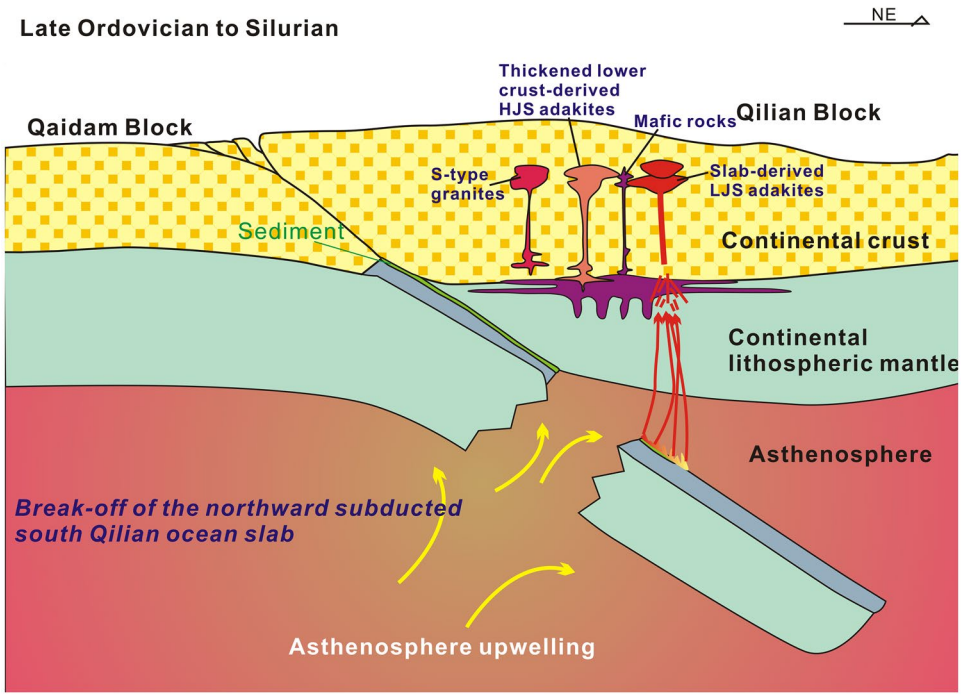

Fig. 12 Schematic illustration of the generation and emplacement of the HJS and LJS adakitic rocks in the eastern Qilian Block

NQ-UHPM belt and Qilian Block may be due to the subduction of a cool oceanic plate and an overall compressional stress regime, which are not favorable for magma ascent (Benito et al. 1999; Eyal et al. 2010). With the South Qilian Ocean closed, a subsequent continental collision between the Qilian and Qaidam Blocks resulted in the Qaidam Block continental lithosphere subducted beneath the Qilian Block, as well as thickening of the Qilian continental crust during the early Ordovician (Zhang et al. 2008). Contrasting behavior of oceanic (negatively buoyant) and continental (positively buoyant) portions of the same lithosphere led to slab break-off after collision in ca. 460 Ma (von Blanckenburg and Davis 1995; Wong et al. 1997). The resultant rapid rise of asthenospheric mantle, in turn, facilitates the extension of the overlying continental lithosphere. The mantle wedge beneath the Qilian Block underwent decompressive melting due to heat flow from the upwelling asthenosphere. It gave rise to the generation of mafic–ultramafic intrusions with arc magmatic geochemical characteristics that are now located in the eastern Qilian Block. Concurrently, hot asthenospheric materials through the slab window would first result in partial melting of the broken edges of the oceanic slab and overlying sediments, then formed the slab-derived LJS adakites, and also induced partial melting of the middle-lower crustal materials through heat conduction to generate the crustal-derived HJS adakitic rocks, and the Xindian and Jishishan S-type granites in the eastern part of the Qilian Block (Fig. 12). With the slab break-off windows widening, the continued upwelling of the asthenospheric mantle then afforded sufficient energy. It gradually propagated northward, resulting in a decrease in the crystallization ages of the granitoids/ S-type granitoids within the Qilian Block trending towards the north. Differences in source compositions and conditions of melting are responsible for the generation of the varying granitoids within the Qilian Block.

Conclusions

New LA–ICP–MS zircon U–Pb dating and whole-rock analysis results indicate that the HJS and LJS granitoids along the southern margin of the Qilian Block were emplaced between 445 and 438 Myr ago and have geochemical characteristics similar to those of adakite. The HJS granites were most likely derived from partial melting of a thickened juvenile lower crust, leaving amphibole and plagioclase residues. In contrast, the LJS quartz diorites were derived from partial melting of subducted oceanic crust and minor oceanic sediments with garnet + rutile + amphibole as residual minerals in the source. By integrating the new results and previous data, it is suggested that the break-off of the northward subducting South Qilian Ocean slab is the most likely geodynamic mechanism for the formation of the HJS and LJS adakitic rocks in the eastern Qilian Block.

Supplementary information The online version contains supplementary material available at https://doi.org/10.1007/s00710-021-00762-y.

Acknowledgements MC–ICP–MS analyses were performed at Wuhan SampleSolution Analytical Technology Co., Ltd. Zircon U–Pb isotopic analyses by ICP–MS and whole-rock major and trace element analyses were conducted at the State Key Laboratory for Mineral Deposits Research, Nanjing University (MiDeR-NJU). Whole-rock Sr–Nd isotopic compositions were determined at Tianjin Shangnuo Geological Technology Co. Ltd. We acknowledge thoughtful comments and constructive suggestions by two anonymous reviewers and editors Xisheng Xu and Lutz Nasdala, which greatly helped to improve the manuscript. This study was financially supported by National Natural Science Foundation of China (Grant 41702048), the Second Tibetan Plateau Scientific Expedition and Research Program (Grant 2019QZKK0704) and the Fundamental Research Funds for the Central Universities (Grant lzujbky-2021-ct07).

References

Andersen T (2002) Correction of common lead in U-Pb analyses that do not report ^{204}Pb. Chem Geol 192:59–79

Anderson JL, Smith DR (1995) The effects of temperature and fO_2 on the Al-in-hornblende barometer. Am Mineral 80(5):549–559

Atherton MP, Petford N (1993) Generation of sodium-rich magmas from newly underplated basaltic crust. Nature 362:144–146

Barbarin B (1999) A review of the relationships between granitoid types, their origins and their geodynamic environments. Lithos 46(3):605–626

Barboni M, Bussy F (2013) Petrogenesis of magmatic albite granites associated to cogenetic A-type granites: Na-rich residual melt extraction from a partially crystallized A-type granite mush. Lithos 177:328–351

Benito R, López-Ruiz J, Cebriá JM, Hertogen J, Doblas M, Oyarzun R, Demaiffe D (1999) Sr and O isotope constraints on source and crustal contamination in the high-K calc-alkaline and shoshonitic neogene volcanic rocks of SE Spain. Lithos 46(4):773–802

Black LP, Gulson BL (1978) The age of the mud tank carbonatite, Strangways range, Northern territory. BMR J Aust Geol Geophys 3:227–232

Boynton WV (1984) Geochemistry of the rare earth elements: meteorite studies. In: Henderson P (ed) Rare Earth Elements Geochemistry. Elservier, Amsterdam, pp. 63–144

Castillo PR (2012) Adakite petrogenesis. Lithos 134–135:304–316

Castillo PR, Janney PE, Solidum RU (1999) Petrology and geochemistry of Camiguin Island, southern Philippines: insights to the source of adakites and other lavas in a complex arc setting. Contrib Mineral Petrol 134:33–51

Chappell BW, White AJR (1974) Two contrasting granite types. Pac Geol 8:173–174

Chen B, Jahn BM, Suzuki K (2013) Petrological and Nd-Sr-Os isotopic constraints on the origin of high-Mg adakitic rocks from the North China Craton: tectonic implications. Geology 41:91–94

Chen JL, Xu XY, Zeng ZX, Xiao L, Wang HL, Wang ZQ, Xiao SW (2008) Geochemical characters and LA-ICPMS zircon U-Pb dating constraints on the petrogenesis and tectonic setting of the Shichuan intrusion, east segment of the Central Qilian, NW China. Acta Petrol Sin 24(4):841–854

Chung SL, Liu D, Ji J, Chu MF, Lee HY, Wen DJ, Lo CH, Lee TY, Qian Q, Zhang Q (2003) Adakites from continental collision zones: melting of thickened lower crust beneath southern Tibet. Geology 31:1021–1024

Conrad WK, Nicholls IA, Wall VJ (1988) Water-saturated and -undersaturated melting of metaluminous and peraluminous crustal compositions at 10 kb: Evidence for the origin of silicic magmas in the Taupo Volcanic Zone, New Zealand, and other occurrences. J Petrol 29(4):765–803

Corfu F, Hanchar JM, Hoskin PW, Kinny P (2003) Atlas of zircon textures. Rev Mineral Geochem 53:469–500

Cui JW, Tian LM, Sun JY, Yang C (2018) Geochronology and geochemistry of early Palaeozoic intrusive rocks in the Lajishan area of the eastern south Qilian Belt, Tibetan Plateau: implications for the tectonic evolution of South Qilian. Geol J 1–17

Dai HK, Zheng JP, Zhou X, Griffin WL (2017) Generation of continental adakitic rocks: Crystallization modeling with variable bulk partition coefficients. Lithos 272–273:222–231

Deer W, Howie R, Zussman J (1992) An Introduction to the Rock-Forming Minerals Longman Scientific and Technical. Essex, UK

Defant MJ, Drummond MS (1990) Derivation of some modern arc magmas by melting of young subducted lithosphere. Nature 347:662–665

Drummond MS, Defant MJ (1990) A model for trondhjemite–tonalite–dacite genesis and crustal growth via slab melting: Archaean to modern comparisons. J Geophys Res 95:21503–21521

Eyal E, Litvinovsky B, John BM, Zanvilevich A, Katzir Y (2010) Origin and evolution of post–collisional magmatism: Coeval Neoproterozoic calc-alkaline and alkaline suites of the Sinai Peninsula. Chem Geol 269:153–179

Eyuboglu Y, Santosh M, Chung SL (2011) Crystal fractionation of adakitic magmas in the crust–mantle transition zone: Petrology, geochemistry and U-Pb zircon chronology of the Seme adakites, eastern Pontides, NE Turkey. Lithos 121:151–166

Foley S, Tiepolo M, Vannucci R (2002) Growth of early continental crust controlled by melting of amphibolite in subduction zones. Nature 417(20):837–840

Foley SF, Wheller GE (1990) Parallels in the origin of the geochemical signatures of island arc volcanics and continental potassic igneous rocks: The role of residual titanites. Chem Geol 85(1–2):1–18

Foster MD (1960) Interpretation of the composition of trioctahedral micas. Geol Surv Prof Pap 354-B:11–49

Frost BR, Barnes CG, Collins WJ, Arculus RJ, Ellis DJ, Frost CD (2001) A geochemical classification for granitic rocks. J Petrol 42:2033–2048

Fu CL, Yan Z (2017) The composition, age and tectonic setting of Lajishan Ophiolitc Mélange. Acta Geosci Sin 38(S1):29–32

Fu CL, Yan Z, Guo XQ, Niu ML, Xia WJ, Wang ZQ, Li JL (2014) Geochemistry and SHRIMP zircon U-Pb age of diabases in the Lajishankou ophiolitic mélange, South Qilian terrane. Acta Petrol Sin 30:1695–1706

Gao JF, Lu JJ, Lin YP, Pu W (2003) Analysis of trace elements in rock samples using HR-ICPMS. Earth Sci J China Univ Geosci 39:844–850 (**(in Chinese with English abstract)**)

Gao S, Rudnick RL, Yuan HL, Liu XM, Liu YS, Xu WL, Lin WL, Ayerss J, Wang XC, Wang QH (2004) Recycling lower continental crust in the North China Craton. Nature 432:892–897

Gao Z, Zhang HF, Yang H, Pan FB, Luo BJ, Guo L, Xu WC, Tao L, Zhang LQ, Wu J (2018) Back-arc basin development: Constraints on geochronology and geochemistry of arc-like and OIB-like basalts in the Central Qilian block (Northwest China). Lithos 310:255–268

Griffin WL, Powell WJ, Pearson NJ, O'Reilly SY (2008) GLITTER: data reduction software for laser ablation ICP-MS. In: Sylvester P (ed) Laser Ablation–ICP–MS in the earth sciences. Mineral Assoc Canada Short Course Series vol 40, Appendix 2, pp 204–207

Guo ZP, Li WY, Zhang ZW, Gao YB, Zhang JW, Li K (2015) Petrogenisis of Lumanshan granites in Hualong area of southern Qilian Mountain: constraints from geochemistry, zircon U-Pb geochronology and Hf isotope. Geology in China 42(4):864–880

Hawkesworth CJ, Turner SP, McDermott F, Peate DW, van Calsteren P (1997) U-Th isotopes in arc magmas: implications for element transfer from subducted crust. Science 276:561–555

He SP, Wang HL, Chen JL, Xu XL, Zhang HF, Ren GM, Yu JY (2008) LA-ICP-MS U-Pb zircon geochronology of basic dikes within Maxianshan rock group in the central Qilian orogenic belt and its tectonic implications. Earth Sci J China Univ Geosci 18:19–29

Hu ZC, Liu YS, Gao S, Liu WQ, Zhang W, Tong XR, Lin L, Zong KQ, Li M, Chen HH (2012) Improved in situ Hf isotope ratio analysis of zircon using newly designed X skimmer cone and jet sample cone in combination with the addition of nitrogen by laser ablation multiple collector ICP-MS. J Anal Atom Spectrom 27:1391–1399

Huang H, Niu Y, Nowell G, Zhao Z, Yu X, Mo X (2015) The nature and history of the Qilian Block in the context of the development of the greater Tibetan plateau. Gondwana Res 28(1):209–224

Irvine TN, Baragar WRA (1971) A guide to the chemical classification of the common volcanic rocks. Can J Earth Sci 8:523–548

Jackson SE, Pearson NJ, Griffin WL, Belousoval EA (2004) The application of laser ablation-inductively coupled plasma-mass spectrometry (LA-ICP-MS) to in situ U-Pb zircon geochronology. Chem Geol 211:47–69

Leake BE, Woolley AR, Arps CES, Birch WD, Gilbert MC, Grice JD, Hawthorne FC, Kato A, Kisch HJ, Krivovichev VG, Linthout K, Laird J, Mandarino J, Maresch WV, Nickel EH, Schumacher JC, Smith DC, Stephenson NCN, Ungaretti L, Whittaker EJW, Youzhi G (1997) Nomenclature of amphiboles: Report of the Subcommittee on Amphiboles of the International Mineralogical Association, Commission on New Minerals and Mineral names. Can Mineral 35:219–246

Li JY, Niu YL, Chen S, Sun WL, Zhang Y, Liu Y, Ma YX, Zhang GR (2017) Petrogenesis of granitoids in the eastern section of the Central Qilian Block: evidence from geochemistry and zircon U-Pb geochronology. Mineral Petrol 111(1):23–41

Li SM, Zhu DC, Wang Q, Zhao Z, Zhang LL, Liu SA (2016) Slab-derived adakites and subslab asthenosphere-derived oib-type rocks at 156 ± 2 ma from the north of gerze, central tibet: records of the bangong–nujiang oceanic ridge subduction during the late Jurassic. Lithos 262:456–469

Li YL, Tong X, Zhu YH, Lin JW, Zheng JP, Brouwer FM (2018) Tectonic affinity and evolution of the Precambrian Qilian block: Insights from petrology, geochemistry and geochronology of the Hualong Group in the Qilian Orogen, NW China. Precambrian Res 315:179–200

Li ZX, Li XH, Chung SL, Lo CH, Xu XS, Li WX (2012) Magmatic switch-on and switch-off along the South China continental margin since the Permian: transition from an Andean-type to a Western Pacific-type plate boundary. Tectonophysics 532–535:271–290

Liégeois JP (1998) Preface– some words on the post-collisional magmatism. Lithos 45:15–17

Liu SA, Li SG, He YS, Huang F (2010a) Geochemical contrasts between early Cretaceous ore-bearing and ore-barren high-Mg adakites in central-eastern China: implications for petrogenesis and Cu–Au mineralization. Geochim Cosmochim Acta 74:7160–7178

Liu YS, Hu ZC, Zong KQ, Gao CG, Gao S, Xu JA, Chen HH (2010b) Reappraisement and refinement of zircon U-Pb isotope and trace element analyses by LA-ICP-MS. Chin Sci Bull 55:1535–1546

Ludwig KR (2003) Isoplot 3.00: A Geochronological Toolkit for Microsoft Excel, Berkeley Geochronology Center. Special publication no. 4

Ma BJ, Wu SG, Fan JK (2015a) An overview of slab window. Mar Geol Front 31:1–10

Ma Q, Xu YG, Zheng JP, Griffin WL, Hong LB, Ma L (2016) Coexisting Early Cretaceous high-Mg andesites and adakitic rocks in the North China Craton: the role of water in intraplate magmatism and cratonic destruction. J Petrol 57(7):1279–1308

Ma Q, Zheng JP, Xu YG, Griffin WL, Zhang RS (2015b) Are continental "adakites" derived from thickened or foundered lower crust? Earth Planet Sci Lett 419:125–133

Macpherson CG, Dreher ST, Thirlwall MF (2006) Adakites without slab melting: high pressure differentiation of island arc magma, Mindanao, the Philippines. Earth Planet Sci Lett 243:581–593

Maniar PD, Piccoli PM (1989) Tectonic Discrimination of Granitoids GSA Bull 101:635–643

Martin H (1999) The adakitic magmas: modern analogues of Archaean granitoids. Lithos 46(3):411–429

Martin H, Smithies RH, Rapp R, Moyen JF, Champion D (2005) An overview of adakite, tonalite-trondhjemite-granodiorite (TTG), and sanukitoid: relationships and some implications for crustal evolution. Lithos 79:1–24

McDonough WF, Sun SS (1995) The composition of the Earth. Chem Geol 120:223–253

Middlemost EAK (1994) Naming materials in the magma/igneous rock system. Earth-Sci Rev 37:215–224

Miller RG, O'Nions RK (1985) Source of Precambrian chemical and clastic sediments. Nature 314:325–330

Moyen JF (2009) High Sr/Y and La/Yb ratios: The meaning of the "adakitic signature." Lithos 112:556–574

Moyen JF, Stevens G (2006) Experimental constraints on TTG petrogenesis: implications for Archean Geodynamics, in: Benn K, Mareschal JC, Condie KC (Eds.) Archean Geodynamics and Environments: Geophysical Monograph 164. American Geophysical Union, Washington, DC

Nagel TJ, Hoffmann E, Münker C (2012) Generation of eoarchean tonalite - trondhjemite - granodiorite series from thickened mafic arc crust. Geology 40(4):375–378

Papoutsa A, Pe-Piper G (2014) Geochemical variation of amphiboles in A-type granites as an indicator of complex magmatic systems: Wentworth pluton, Nova Ccotia, Canada. Chem Geol 384:120–134

Peccerillo A, Taylor DR (1976) Geochemistry of Eocene calc-alkaline volcanic rocks from the Kaitamonu area, Northern Turkey. Contrib Mineral Petrol 58:63–91

Peng YB, Yu SY, Zhang JX, Li SZ, Tong LX, Sun DY, Tong LX, Sun DY (2017) Early paleozoic arc magmatism and metamorphism in the northern qilian block, western china: petrological and geochronological constraints. Geol J 52(S1):339–364

Prouteau G, Scaillet B, Pichavant M, Maury R (2001) Evidence for mantle metasomatism by hydrous silicic melts derived from subducted oceanic crust. Nature 40:197–200

Qin HP, Wu CL, Wang CS, Lei M, Liu CH, Li MZ (2014) LA-ICP- MS zircon U- Pb characteristical of Xiagucheng granite in North Qilian. Acta Geol Sin 88(10):1832–1842

Rapp RP, Long X, Shimizu N (2002) Experimental constraints on the origin of potassium-rich adakites in eastern China. Acta Petrol Sin 18:293–302

Richards JP (2011) High Sr/Y arc magmas and porphyry Cu ± Mo ± Au deposits: Just add water. Econ Geol 106(7):1075–1081

Richards JP (2015) Tectonic, magmatic, and metallogenic evolution of the Tethyan orogen: From subduction to collision. Ore Geol Rev 70:323–345

Ridolfi F, Renzulli A, Puerini M (2010) Stability and chemical equilibrium of amphibole in calc-alkaline magmas: an overview, new thermobarometric formulations and application to subduction-related volcanoes. Contrib Mineral Petrol 160:45–66

Sen C, Dunn T (1994) Dehydration melting of a basaltic composition amphibolite at 1.5 and 2.0 GPa: implications for the origin of adakites. Contrib Mineral Petrol 117:394–409

Shi RD, Yang JS, Wu CL, Iizuka T, Hirata T (2006) Island arc volcanic rocks in the North Qaidam UHP belt, northern Tibet Plateau:

evidence for ocean–continent subduction preceding continent–continent subduction. J Asian Earth Sci 28:151–159
Song SG, Niu YL, Su L, Wei CJ, Zhang LF (2014a) Adakitic (tonalitic-trondhjemitic) magmas resulting from eclogite decompression and dehydration melting during exhumation in response to continental collision. Geochim Cosmochim Acta 130:42–62
Song SG, Niu YL, Su L, Xia XH (2013) Tectonics of the North Qilian orogen. NW China Gondwana Res 23(4):1378–1401
Song SG, Niu YL, Su L, Zhang C, Zhang LF (2014b) Continental orogenesis from ocean subduction, continent collision/subduction, to orogen collapse, and orogen recycling: the example of the North Qaidam UHPM belt, NW China. Earth-Sci Rev 129:59–84
Song SG, Niu YL, Zhang LF, Wei CJ, Liou JG, Su L (2009) Tectonic evolution of early Paleozoic HP metamorphic rocks in the North Qilian Mountains, NW China: new perspectives. J Asian Earth Sci 35:334–353
Stern CR, Kilian R (1996) Role of the subducted slab, mantle wedge and continental crust in the generation of adakites from the Andean austral volcanic zone. Contrib Mineral Petrol 123:263–281
Streck MJ, Leeman WP, Chesley J (2007) High-magnesian andesite from Mount Shasta: a product of magma mixing and contamination, not a primitive mantle melt. Geology 35:351–354
Tao L, Zhang HF, Yang H, Gao Z, Pan FB, Luo BJ (2018) Initial back-arc extension: evidence from petrogenesis of early Paleozoic MORB-like gabbro at the southern Central Qilian block, NW China. Lithos 322:166–178
Tatsumi Y, Hanyu T (2003) Geochemical modeling of dehydration and partial melting of subducting lithosphere: toward a comprehensive understanding of high-Mg andesite formation in the Setouchi volcanic belt. SW Japan Geochem Geophys Geosyst 4(9):1–19
Tung KA, Yang HY, Liu DY, Zhang JX, Yang HJ, Shau YH, Tseng CY (2013) The Neoproterozoic granitoids from the Qilian block, NW China: evidence for a link between the Qilian and South China Blocks. Precambrian Res 235:163–189
Tung KA, Yang HY, Liu DY, Zhang JX, Yang HJ, Shau YH, Tseng CY (2012) The amphibolite-facies metamorphosed mafic rocks from the Maxianshan area, Qilian block, NW China: a record of early Neoproterozoic arc magmatism. J Asian Earth Sci 46:177–189
Tung KA, Yang HY, Yang HJ, Smith A, Liu D, Zhang J (2016) Magma sources and petrogenesis of the early-middle paleozoic backarc granitoids from the central part of the Qilian Block, NW china. Gondwana Res 38:197–219
von Blanckenburg F, Huw Davies J (1995) Slab breakoff: a model for syncollisional magmatism and tectonics in the Alps. Tectonics 14:120–131
Wan YS, Xu ZQ, Yang JS, Zhang JX (2003) The Precambrian high-grade basement of the Qilian Terrane and neighboring areas: its age and compositions. Acta Geol Sin 24:319–324
Wang J, Kéiko H, Hattori KR, Stern CR (2007a) Metasomatism of sub-arc mantle peridotites below southernmost South America: reduction of fO_2 by slab-melt. Contrib Mineral Petrol 153(5):607–624
Wang KX, Yu CD, Yan J, Liu XD, Liu WH, Pan JY (2019) Petrogenesis of Early Silurian granitoids in the Longshoushan area and their implications for the extensional environment of the North Qilian Orogenic Belt, China. Lithos 342–343:152–174
Wang N, Wu CL, Lei M, Chen HJ (2018) Petrogenesis and tectonic implications of the Early Paleozoic granites in the western segment of the North Qilian orogenic belt, China. Lithos 312–313:89–107
Wang Q, Li XH, Jia XH, Wyman D, Tang GJ, Li ZX, Ma L, Yang YH, Jiang ZQ, Gou GN (2012) Late Early Cretaceous adakitic granitoids and associated magnesian and potassium-rich mafic enclaves and dikes in the Tunchang-Fengmu area, Hainan Province (South China): partial melting of lower crust and mantle, and magma hybridization. Chem Geol 328:222–243
Wang Q, Wyman DA, Xu JF, Zhao ZH, Jian P, Xiong XL, Bao ZW, Li CF, Bai ZH (2006a) Petrogenesis of Cretaceous adakitic and shoshonitic igneous rocks in the Luzong area, Anhui Province (Eastern China): implications for geodynamics and Cu–Au mineralization. Lithos 89:424–446
Wang Q, Wyman DA, Xu JF, Jian P, Zhao ZH, Li C, Xu W, Ma JL, He B (2007b) Early Cretaceous adakitic granites in the Northern Dabie Complex, central China: implications for partial melting and delamination of thickened lower crust. Geochim Cosmochim Acta 71:2609–2636
Wang Q, Xu JF, Jian P, Bao ZW, Zhao ZH, Li CF, Xiong XL, Ma JL (2006b) Petrogenesis of adakitic porphyries in an extensional tectonic setting, Dexing, South China: implications for the genesis of porphyry copper mineralization. J Petrol 47:119–144
Wang T, Wang Z, Yan Z, Ma Z, He S, Fu C, Wang D (2016) Geochronological and Geochemical evidence of amphibolite from the Hualong Group, northwest China: implication for the early Paleozoic accretionary tectonics of the Central Qilian belt. Lithos 248:12–21
Whitney DL, Evan BW (2010) Abbreviations for names of rock-forming minerals. Am Mineral 95:18–187
Wong A, Ton SYM, Wortel MJR (1997) Slab detachment in continental collision zones: an analysis of controlling parameters. Geophys Res Lett 24:2095–2098
Woodhead JD, Hergt JM, Davidson JP, Eggins SM (2001) Hafnium isotope evidence for 'conservative' element mobility during subduction zone processes. Earth Planet Sci Lett 192(3):331–346
Wu CL, Xu XY, Gao QM, Li XM, Lei M, Gao YH, Frost RB, Wooden JL (2010) Early Palaezoie granitoid magmatism and tectonic evolution in North Qilian, NW China. Acta Petrol Sin 26:1027–1044
Wu FY, Sun DY, Li HM, Jahn BM, Wilde S (2002) A-type granites in northeastern China: age and geochemical constraints on their petrogenesis. Chem Geol 234(1–2):105–126
Wu FY, Yang YH, Xie LW, Yang JH, Xu P (2006) Hf isotopic compositions of the standard zircons and baddeleyites used in U-Pb geochronology. Chem Geol 234:105–126
Wu YB, Zheng YF (2004) Genesis of zircon and its constraints on interpretation of U-Pb age. Chin Sci Bull 49:1554–1569
Xia LQ, Li XM, Yu JY, Wang GQ (2016) Mid−Late Neoproterozoic to Early Paleozoic volcanism and tectonic evolution of the Qilian Mountain. Geology in China 43(4):1087–1138
Xiong Q, Zheng JP, Griffin WL, O'Reilly SY, Zhao JH (2011) Zircons in the Shenglikou ultrahigh-pressure garnet peridotite massif and its country rocks from the North Qaidam terrane (western China): Meso-Neoproterozoic crust–mantle coupling and early Paleozoic convergent plate-margin processes. Precambrian Res 187:33–57
Xiong XL, Adam J, Green TH (2005) Rutile stability and rutile/melt HFSE partitioning during partial melting of hydrous basalt: implications for TTG genesis. Chem Geol 218:339–359
Xu JF, Shinjo R, Defant MJ, Wang QA, Rapp RP (2002) Origin of Mesozoic adakitic intrusive rocks in the Ningzhen area of east China: Partial melting of delaminated lower continental crust? Geology 30:1111–1114
Xu WC (2007) U-Pb Zircon Geochronology, Geochemical and Sr-Nd-Hf Isotopic Compositions of the Hualong Group in Qilian Mountains: Constraints on Tectonic Evolution of Crustal Basement. China University of Geosciences, Wuhan, pp 20–21
Xu ZQ, Yang JS, Wu CL, Li HB, Zhang JX, Qi XX, Song SG, Qiu HJ (2006) Timing and mechanism of formation and exhumation of the Northern Qaidam ultrahighpressure metamorphic belt. J Asian Earth Sci 28:160–173
Yan Z, Aitchison J, Fu CL, Guo XQ, Niu ML, Xia WJ, Li JL (2015) Hualong Complex, South Qilian terrane: U-Pb and

Lu–Hf constraints on Neoproterozoic micro-continental fragments accreted to the northern Proto-Tethyan margin. Precambrian Res 266:65–85

Yang H, Zhang H, Luo B, Gao Z, Guo L, Xu W (2016) Generation of peraluminous granitic magma in a post-collisional setting: a case study from the eastern Qilian Orogen, NE Tibetan plateau. Gondwana Res 36:28–45

Yang H, Zhang HF, Luo BJ, Zhang J, Xiong ZL, Guo L, Pan FB (2015) Early Paleozoic intrusive rocks from the eastern Qilian orogen, NE Tibetan Plateau: petrogenesis and tectonic significance. Lithos 224:13–31

Yang H, Zhang HF, Luo BJ, Gao Z, Tao L (2018) Petrogenesis of early Paleozoic diorites and mafic-intermediate dykes from the eastern Qilian orogen, NE Tibetan Plateau: implication for lithospheric processes. J Geol Soc Lond 175:525–542

Yang H, Zhang HF, Xiao WJ, Tao L, Gao Z, Luo BJ, Zhang LQ (2021) Multiple Early Paleozoic granitoids from the southeastern Qilian orogen, NW China: Magma responses to slab roll-back and break-off. Lithos 380–381: 105910

Yang JS, Xu ZQ, Li HB, Wu CL, Cui JW, Zhang JX, Chen W (1998) Discovery of eclogite at northern margin of Qaidam Basin, NW China. Chin Sci Bull 43:1755–1760

Yong Y, Xiao WJ, Yuan C, Yan Z, Li JL (2008) Geochronology and geochernistry of Paleozoic granitic plutons from the eastern Central Qilian and their tectonic implications. Acta Petrol Sin 24:855–866

Yu JY, Li XM, Ma ZP, Wang GQ, Tang Z, Sun JM, Wu P (2012) Zircon U-Pb dating of the Yishichun mafic–ultramafic complex in southern Qilian and its geological significance. Geol J China Univ 18:158–163

Zhang GB, Song SG, Zhang L, Niu YL (2008) The subducted oceanic crust within continental-type UHP metamorphic belt in the North Qaidam, NW China: evidence from petrology, geochemistry and geochronology. Lithos 104:99–118

Zhang HF, Jin LL, Zhang L, Yuan HL, Zhou L, Zhang BR (2006) Pb and Nd isotopic compositions of basement and granitoid in the Qilianshan: constraints on tectonic affinity. Earth Sci J China Univ Geosci 31(1):57–65

Zhang Q, Wang Y, Qian Q, Yang JH, Wang YL, Zhao TP, Guo GJ (2001) The characteristics and tectonic–metallogenic significances of the adakites in Yanshan period from eastern China. Acta Petrol Sin 17:236–244

Zhang YQ, Song SG, Yang LM, Su L, Niu YL, Allen MB, Xu X (2017) Basalts and picrites from a plume-type ophiolite in the South Qilian accretionary belt, Qilian Orogen: accretion of a Cambrian oceanic plateau? Lithos 278–281:97–110

Zhang ZW, Li WY, Gao YB, Li C, Ripley EM, Kamo S (2014) Sulfide mineralization associated with arc magmatism in the Qilian Block, western China: zircon U-Pb age and Sr–Nd–Os–S isotope constraints from the Yulonggou and Yaqu gabbroic intrusions. Mineral Deposita 49:279–292

Zhang ZW, Li WY, Wang YL, Gao YB (2015) The genesis study on Xiashentang basic-ultrabasic intrusion associated with Ni-Cu mineralization in Hualong, Southern Qilian Mountains: zircon geochronology, geochemistry and Sr-Nd isotopic constraints. Acta Petrol Sin 31(9):2539–2548

Zhao JH, Zhou MF (2007) Neoproterozoic adakitic plutons and arc magmatism along the western margin of the Yangtze block, South China. J Geol 115:675–689

Zhu KY, Li ZX, Xu XS, Wilde SA (2014) A Mesozoic Andean-type orogenic cycle in southeastern China as recorded by granitoid evolution. Am J Sci 314:187–234